

Yu-Shiba-Rusinov states in the charge-density modulated superconductor NbSe₂

Eva Liebhaber,¹ Sergio Acero González,² Rojhat Baba,¹ Gaël Reecht,¹ Benjamin W. Heinrich,¹
Sebastian Rohlf,^{3,4} Kai Rossnagel,^{3,4,5} Felix von Oppen,² and Katharina J. Franke¹

¹*Fachbereich Physik, Freie Universität Berlin, 14195 Berlin, Germany*

²*Dahlem Center for Complex Quantum Systems and Fachbereich Physik, Freie Universität Berlin, 14195 Berlin, Germany*

³*Institut für Experimentelle und Angewandte Physik, Christian-Albrechts-Universität zu Kiel, 24098 Kiel, Germany*

⁴*Ruprecht-Haensel-Labor, Christian-Albrechts-Universität zu Kiel, 24098 Kiel, Germany*

⁵*Deutsches Elektronen-Synchrotron DESY, 22607 Hamburg, Germany*

(Dated: July 12, 2022)

At low temperatures, charge-density-wave and superconducting order coexist in the quasi-two-dimensional material 2H-NbSe₂. Here, we investigate the Yu-Shiba-Rusinov (YSR) states of individual Fe atoms adsorbed in hollow sites of the terminating Se surface. We find that the charge density wave (CDW) strongly modifies both the wavefunctions and the energies of the YSR states. Exploiting the incommensurate nature of the CDW, we can trace the YSR states as a function of adsorption site relative to the CDW in a detailed manner. Key features are reproduced in model calculations. Our results emphasize the importance of the detailed atomic-scale environment for the design of nanostructures from coupled YSR adsorbates.

Paramagnetic adatoms act as a local pair-breaking potential on the Cooper pairs of a superconducting substrate. This induces low-energy bound states in the superconducting energy gap which are known as Yu-Shiba-Rusinov (YSR) states [1–3]. Rich spectra of YSR states have been observed for transition metal atoms such as Cr, Mn, or Fe on bulk superconductors [4–9]. Multiplets of YSR states arise from a lifting of *d*-level degeneracies in response to the local crystal field of the adsorption site [10]. The spatial symmetry of YSR states is determined by the crystal field and is directly reflected in the observed YSR patterns around the adatom [7]. The patterns are further affected by the superconducting host. Electrons scattered by an impurity are focused along directions that are perpendicular to flat sections of the host’s Fermi surface. This focusing dominates the symmetry of the YSR patterns in the far field [11, 12], and partially offsets the rapid $1/r$ -decay of the YSR wavefunctions in an isotropic bulk superconductor [3].

In two-dimensional superconductors, YSR wavefunctions are predicted to decay more slowly away from the adatom even for isotropic Fermi surfaces, obeying a $1/r^{1/2}$ -dependence. Consistent with this expectation, Ménard *et al.* [13] found that YSR states around buried Fe impurities in the layered superconductor 2H-NbSe₂ ($T_c \approx 7.2$ K) can be resolved up to several nm away from the impurity. As observed in Ref. [14], the slow decay of the YSR states also enhances the hybridization of YSR states of nearby impurities. Moreover, the coupling is predicted to be highly directional, due to the electron focusing, thus highlighting the importance of understanding the scattering patterns around magnetic adsorbates [14–16].

Here, we focus on the interplay between YSR states and another remarkable aspect of 2H-NbSe₂. Superconductivity in this material coexists with a charge-density wave (CDW) that forms below a critical temperature

of $T_{\text{cdw}} \approx 33$ K and arises from momentum-dependent electron-phonon interactions [17–28]. Its charge-density modulations are incommensurate with the underlying atomic lattice ($a_{\text{cdw}} \gtrsim 3a_{\text{lattice}}$). Adsorption sites which are identical relative to the atomic lattice may thus be inequivalent with respect to the CDW. We show that both the symmetry and the energy of the YSR states of individual Fe atoms adsorbed on 2H-NbSe₂ depend considerably on the precise adsorption position relative to the CDW.

Bulk crystals of 2H-NbSe₂ are grown by iodine vapor transport [21]. A clean surface is prepared by cleaving the crystal in ultra-high vacuum. Single Fe atoms are deposited at temperatures below 12 K into the scanning tunneling microscope (STM) chamber. Measurements are carried out in a Joule-Thomson STM at a temperature of 1.1 K. Scanning tunneling spectroscopy is performed by standard lock-in techniques. To improve the energy resolution beyond the Fermi-Dirac limit, we use superconducting Pb tips. The convolution of the densities of states (DOS) of tip and substrate shifts all spectral features by the energy gap $\Delta_t \approx 1.35$ meV of the tip.

STM images of a clean 2H-NbSe₂ surface show the atomic corrugation with superimposed modulation of the local DOS imposed by the CDW (Fig. 1a). The phase of the CDW relative to the atomic lattice varies smoothly across the surface. Figures 1b,c present two extremal cases for which the maxima coincide either with a Se atom (chalcogenide-centered, CC, Fig. 1d) or a hollow site (hollow-centered, HC, Fig. 1d) [29]. The deposited Fe atoms appear as two stable species with different apparent heights (Fig. 1e,f). By atomic-resolution imaging (for details see Supplemental Material (SM) [30]), we assign adatoms with small (large) apparent height to adsorption in HC (metal-centered, MC) sites, *i.e.* to hollow sites of the terminating Se layer (Fig. 1d) [31].

The superconducting energy gap of the substrate is

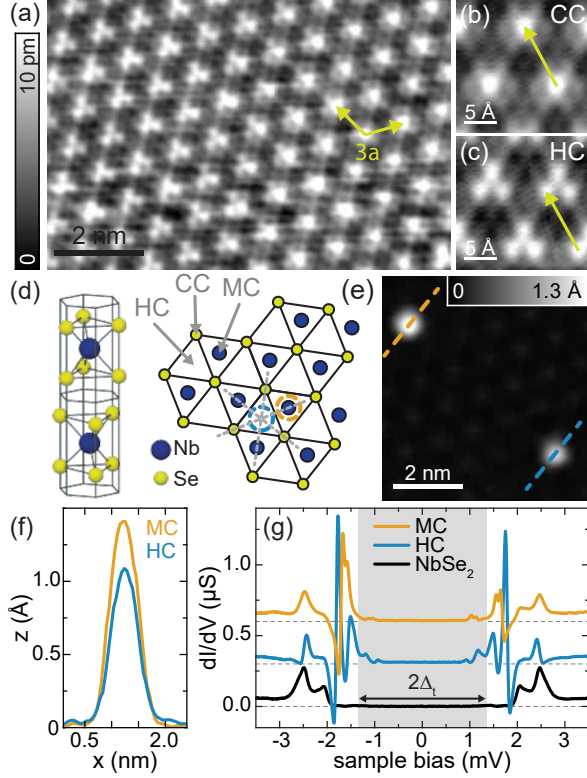


Figure 1. (a) Atomic-resolution STM images showing the incommensurate CDW modulation (constant-current mode with set point 4 mV, 200 pA). (b,c) Close-ups of different regions in (a). (d) Unit cell and top view of $2H$ -NbSe₂, with different lattice sites labeled as HC, CC and MC. Grey dashed lines indicate mirror axes for adatoms (shown for HC site only). (e) Topography of HC and MC adatoms. (f) Line profiles across the atoms shown in (e). (g) Constant-height dI/dV spectra taken on the substrate (black) and on the atoms shown in (e) (set point 4 mV, 200 pA, $V_{rms} = 15 \mu\text{eV}$, offset of $0.3 \mu\text{S}$ for clarity). $2\Delta_t$ is indicated by shaded area.

framed by a characteristic structure of the coherence peaks in an energy range of $2.0 - 2.7 \text{ meV}$ (black dI/dV spectrum in Fig. 1g). The origin of this peculiar quasi-particle DOS has been discussed in terms of multiband or anisotropic superconductivity [32–38]. dI/dV spectra taken above the centers of HC and MC adatoms (blue and orange in Fig. 1g) show several YSR states inside the superconducting gap as well as in the energy range of the substrate’s coherence peaks as has been observed previously for buried impurities [39]. The energy and intensity of the YSR states differ between the two species. Presumably, the splitting of the adatom d -levels is sensitive to the different local environments of the adsorption sites, which in turn affects the potential- and exchange-scattering strengths [7].

In the following, we focus on Fe atoms which are all sitting in the same atomic adsorption site (HC) and show how the properties of the YSR states are influenced by the CDW. Six different atoms (labeled by I-VI) are shown

in Fig. 2a. The corresponding dI/dV spectra (Fig. 2b) reveal that the energy and intensity of their YSR states differ strongly even though their atomic adsorption sites are identical with respect to the unperturbed lattice.

YSR states in the energy range of the superconducting coherence peaks are difficult to disentangle from the background. To avoid this complication, we focus on deep-lying YSR states, specifically the two lowest YSR pairs labeled as $\pm\alpha$ and $\pm\beta$ in the close-up view presented in Fig. 2c. dI/dV maps recorded at the corresponding bias voltages V_α and V_β are shown in Fig. 3a for adatoms I-VI. The main panels show the extended patterns while the insets focus on the immediate vicinity of the adatom. All extended maps show patterns with oscillating intensity [40]. The overall symmetries of the patterns clearly differ between adatoms I-VI.

The symmetry of the patterns associated with YSR states is expected to originate from the anisotropy of the Fermi surface [11] and the local crystal field [7]. The threefold symmetric atomic adsorption site together with the sixfold symmetry of the Fermi surface should therefore lead to D_3 symmetry (threefold rotation as well as three mirror axes, cf. dashed lines in 1d). Interestingly, this D_3 symmetry is observed for both YSR states α and β of adatoms I and III, which reside at a maximum and a minimum of the CDW, respectively (Figs. 2d, 3a). However, this symmetry is lost in both, the long-range and the immediate vicinity of the adatoms for the other atoms shown in Fig. 3a. For adatoms II, IV, and V, the symmetry is reduced to D_1 symmetry (single mirror axis) while no symmetry axis can be discerned for adatom VI.

The symmetry reductions of the YSR patterns coincide with the reductions of the local symmetry of the adsorption sites by the CDW (Fig. 2d). Adatoms I and III are positioned at a maximum or a minimum of the CDW, so that the CDW respects the atomic D_3 symmetry (HC structure of the CDW). Atoms II, IV, and V are located on one of the three equivalent symmetry axes connecting the high-symmetry positions, but unlike adatoms I and III do not directly fall on an extremum (CDW in the CC domain). Thus, the CDW breaks the atomic D_3 symmetry, leaving only D_1 symmetry consistent with the observed YSR patterns. Finally, the position of adatom VI is totally asymmetric with respect to the CDW, which is reflected in the absence of any symmetry in the corresponding dI/dV maps.

The microscopic physics behind these symmetry reductions can be understood theoretically within a phenomenological mean-field description of the CDW combined with a tight-binding model of the $2H$ -NbSe₂ band structure. Foregoing a realistic description of the Fe d -orbital physics, we model the adatom as a classical impurity with isotropic potential and exchange couplings to the substrate (see SM [30] for details). Due to the electron-phonon interaction, the CDW acts on the electrons as a weakly incommensurate, static periodic po-

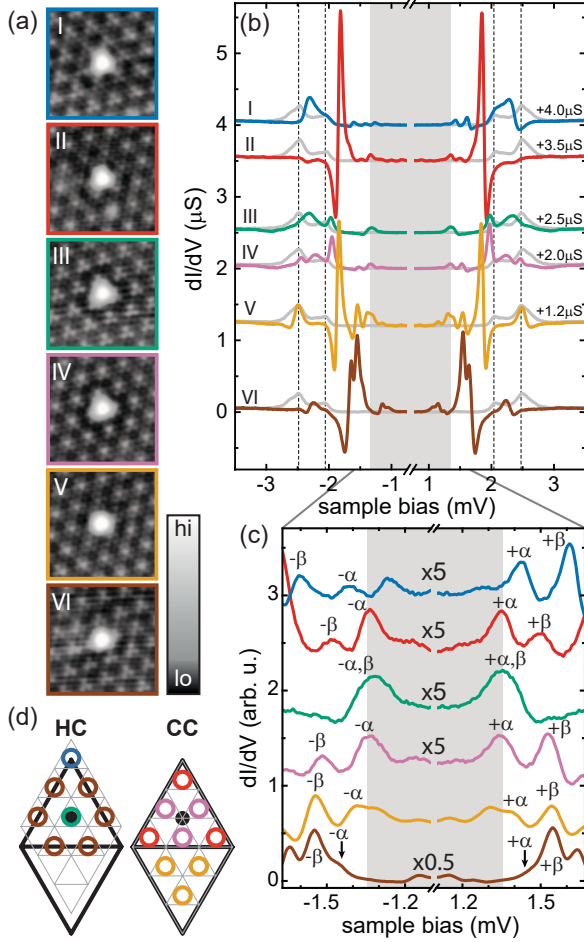


Figure 2. (a) Constant-current STM images ($5 \times 5 \text{ nm}^2$) of several HC Fe atoms labeled by I-VI. A non-linear color code is used to resolve the atomic background (set point: 4 mV, 200 pA). (b) Constant-height dI/dV spectra taken at the center of atoms I-VI (color) and on the substrate (grey). Spectra are offset for clarity. (c) Close-ups of the spectra in (b) scaled as indicated. YSR resonances are labeled by $\pm\alpha, \pm\beta$. (d) Superimposed atomic (grey) and CDW lattices (black) for two CDW structures (HC and CC). The Se atoms are located at vertices of the atomic grids, so that the HC (MC) adsorption sites correspond to triangles pointing up (down). In the CDW lattice, vertices (dots) are maxima (minima) of the CDW. Colored circles indicate the positions of atoms I-VI relative to the CDW.

tential. This potential reduces the symmetry of the YSR wavefunctions in a manner consistent with the experimental results. Corresponding numerical results are shown in Fig. 3c for a subset of the adsorption sites investigated experimentally (see [30] for the remaining sites and further details). We find that the wavefunctions (and the number) of the YSR states are quite sensitive to details of the band structure and the neglected d -orbital physics, so that one expects agreement only for qualitative aspects of symmetry.

So far, the assignments α and β for the YSR states

simply refer to the two deepest resonances. Analyzing the observed YSR patterns allows us to track these two YSR states as a function of position relative to the CDW. For the YSR state $+\beta$ of adatom I, the pattern around the center of the atom we observe a short-range pattern which exhibits a triangular shape (Fig. 3b) with high intensity on its sides and slightly smaller intensity at its vertices (orange circles). In contrast, the YSR state $+\alpha$ for adatom I lacks intensity at the vertices (blue circles) and thus exhibits pronounced nodes. Signatures of this distinction persist at the lower-symmetry positions II, IV, and V. While the intensity distributions change for both states, we still observe distinct intensities at one of the vertices which distinguish between the $+\alpha$ and $+\beta$ resonances (while present, the distinction is somewhat less pronounced for adatom V, for more details see SM [30]). A similar distinction cannot be made for adatom III. We attribute this to the fact that in this case, both the $\pm\alpha$ - and the $\pm\beta$ -resonances lie very close to the Fermi level. This prevents us from individually resolving them within our energy resolution (cf. Fig. 2c, green trace).

With these characteristics, we can track the resonances as a function of position relative to the CDW and probe the effect of the CDW on the YSR energies. As the CDW transforms smoothly between HC and CC structures, we can study numerous positions along a symmetry axis of the CDW (such as positions II, IV, and V in Fig. 2d, but also in between). Altogether, we analyze approximately 90 adatoms adsorbed close to one of the three equivalent CDW symmetry axes, combining data from several samples and Pb tips. For all adatoms, we extract the energies of the YSR states by deconvolving the dI/dV spectra to remove the influence of the Pb tip (see SM [30]). Figure 4a plots the energies of both the α and β states as a function of adatom position along a high-symmetry axis of the CDW. Here, we assume that the energy of the α resonance changes sign, crossing the quantum phase transition [8, 41–43], so that the energy dependences of both resonances follow the same trend. Some regions (shaded in Fig. 4a) of adatom positions remain inaccessible for Fe atoms in HC sites, because the CDW maxima avoid MC domains [29].

A qualitatively similar dependence of the energy of the YSR states is found in our model calculations (Fig. 4c and [30]). The YSR energies are (anti)correlated with the CDW potential and the local DOS, with the type of correlation depending on whether the impurity is in the weak- or strong-coupling regime and on the strength of potential scattering by the impurity [30]. (We find that the CDW potential is anticorrelated with the local DOS.) Unless the potential scattering is surprisingly strong (see [30]), our results are consistent with a simple model for the energy of YSR states [1–3],

$$E_{\text{YSR}} = \pm \Delta \frac{1 - (\pi J S \nu_0 / 2)^2}{1 + (\pi J S \nu_0 / 2)^2}. \quad (1)$$

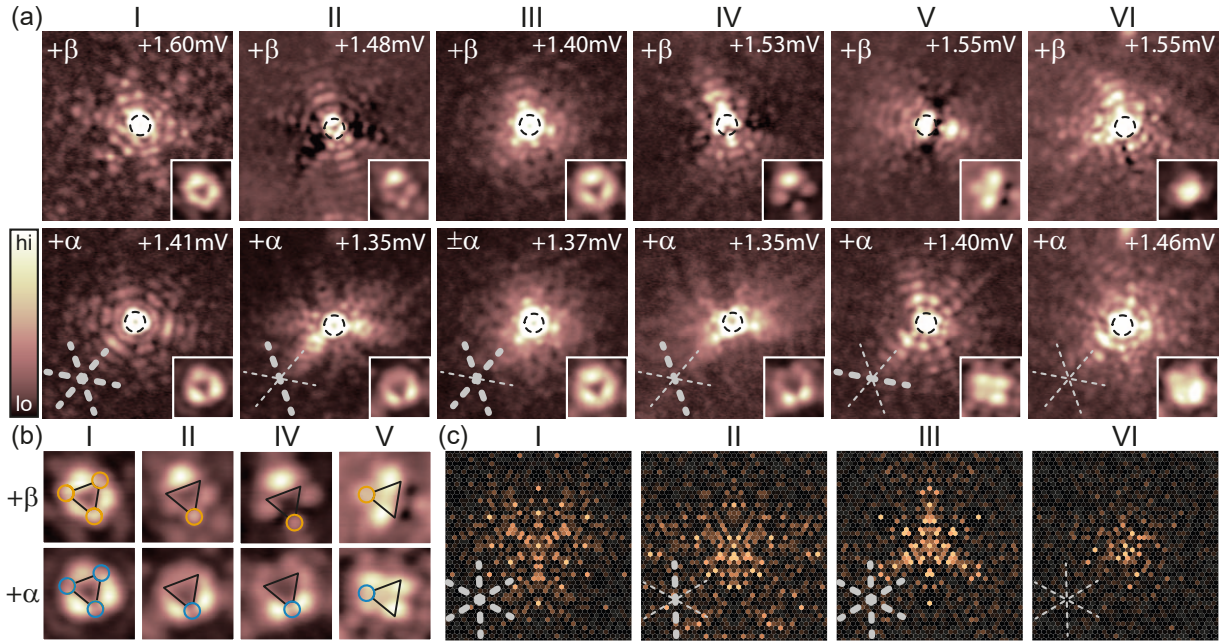


Figure 3. (a) Constant-current dI/dV maps ($9.5 \times 9.5 \text{ nm}^2$) of the YSR (α, β) states of HC atoms (I-VI) (set point: 4 mV, 200 pA; $V_{\text{rms}} = 15\text{-}25 \text{ } \mu\text{eV}$; V_{bias} as indicated in the images). Black dashed circles (diameter 1 nm) outline the atoms' position. The insets show a $2 \times 2 \text{ nm}^2$ close-up view around the center of the atoms. (b) Close-up view around the center of the atoms I, II, IV, and V with superimposed triangles illustrating the presence (orange circles) and absence (blue circles) of intensity at their vertices. On atom III, states α and β overlap, on atom VI there is no symmetry. (c) Numerical results for YSR states within a phenomenological description of the CDW (field of view: $40a \times 40a$ around adatom). For details of the model and parameters, see SM [30], specifically Fig. S3 where these plots are complemented by additional adsorption sites. Thick (thin) grey lines in the maps of each atom indicate presence (absence) of mirror axes in the images.

Here, Δ is the superconducting gap, S the (classical) spin, J the exchange coupling, and ν_0 the local DOS of the superconductor. This predicts that YSR energies are (anti)correlated with the local DOS for impurities in the strong (weak) coupling limit. Experimentally, we extract the modulations in the local DOS due to the CDW from an FFT-filtered constant-height dI/dV map, recorded at the Fermi level above T_c . We find that the YSR energies correlate with the local DOS as seen in Fig. 4a,b. This suggests that the YSR states are in the strong-coupling regime beyond the quantum phase transition to a screened impurity spin.

In conclusion, we find that the CDW affects the properties of YSR states. The CDW modulates the energies of YSR states and reduces the symmetry of the scattering patterns, both in the immediate vicinity of and further from the atoms. This physics is crucial for the design of coupled YSR states as their hybridization is strongest for degenerate YSR states with large wavefunction overlap. Interestingly, the CDW is also present in single-layer NbSe_2 [44, 45]. Our results remain equally important for these truly two-dimensional systems for which pairing correlations are remarkably robust against in-plane fields as a consequence of spin-valley locking (Ising superconductivity) [44]. In view of our result that the YSR states interact with both superconductivity and charge-density

order, they constitute a highly local sensor of these competing interactions and promise insights towards fully unraveling the underlying pairing mechanisms [46].

Financial support by Deutsche Forschungsgemeinschaft through grant CRC 183 (FvO), as well as by the European Research Council through the consolidator grant “NanoSpin” (KJF) is gratefully acknowledged.

-
- [1] L. Yu, *Acta Phys. Sin.* **21**, 75 (1965).
 - [2] H. Shiba, *Prog. Theor. Phys.* **40**, 435 (1968).
 - [3] A.I. Rusinov, *Zh. Eksp. Teor. Fiz. Pisma Red.* **9**, 146 (1968) [*JETP Lett.* **9**, 85 (1969)].
 - [4] A. Yazdani, B. A. Jones, C. P. Lutz, M. F. Crommie, and D. M. Eigler, *Science* **275**, 1767 (1997).
 - [5] S.-H. Ji, T. Zhang, Y.-S. Fu, X. Chen, X.-C. Ma, J. Li, W.-H. Duan, J.-F. Jia, and Q.-K. Xue, *Phys. Rev. Lett.* **100**, 226801 (2008).
 - [6] M. Ruby, F. Pientka, Y. Peng, F. von Oppen, B. W. Heinrich, and K. J. Franke, *Phys. Rev. Lett.* **115**, 087001 (2015).
 - [7] M. Ruby, Y. Peng, F. von Oppen, B. W. Heinrich, and K. J. Franke, *Phys. Rev. Lett.* **117**, 186801 (2016).
 - [8] D.-J. Choi, C. Rubio-Verdú, J. De Bruijkere, M. M. Ugeda, N. Lorente, and J. I. Pascual, *Nature Comm.* **8**, 15175 (2017).

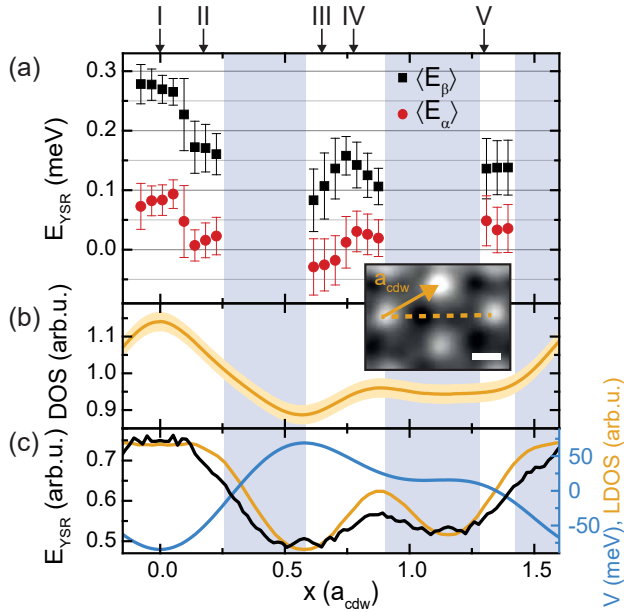


Figure 4. (a) Evolution of the α -, β -YSR energy with the position relative to the CDW. Displayed points are obtained from averaging the energies of various atoms within position intervals of $x \pm 0.05 a_{\text{cdw}}$. Error bars include standard deviation from the averaging method, experimental errors and errors originating from the data processing (see SM [30]). (b) Linecut (orange) through a FFT-filtered constant-height map shown as inset (scale bar is 4 Å) representing the variation of the local DOS. (c) CDW potential (blue), local DOS (orange) and YSR energies (black) obtained from the theoretical model for $JS/2 = 360$ meV, *i.e.*, in the strong-coupling regime.

- [9] L. Cornils, A. Kamlapure, L. Zhou, S. Pradhan, A. A. Khajetoorians, J. Fransson, J. Wiebe, and R. Wiesendanger, *Phys. Rev. Lett.* **119**, 197002 (2017).
- [10] C. P. Moca, E. Demler, B. Jankó, and G. Zaránd, *Phys. Rev. B* **77**, 174516 (2008).
- [11] M. I. Salkola, A. V. Balatsky, and J. R. Schrieffer, *Phys. Rev. B* **55**, 12648 (1997).
- [12] M. E. Flatté and J. M. Byers, *Phys. Rev. Lett.* **78**, 3761 (1997).
- [13] G. C. Ménard, S. Guissart, C. Brun, S. Pons, V. S. Stolyarov, F. Debontridder, M. V. Leclerc, E. Janod, L. Cario, D. Roditchev, P. Simon, and T. Cren, *Nature Phys.* **11**, 1013 (2015).
- [14] S. Kezilebieke, M. Dvorak, T. Ojanen, and P. Liljeroth, *Nano Lett.* **18**, 2311 (2018).
- [15] M. Ruby, B. W. Heinrich, Y. Peng, F. von Oppen, and K. J. Franke, *Phys. Rev. Lett.* **120**, 156803 (2018).
- [16] D.-J. Choi, C. G. Fernández, E. Herrera, C. Rubio-Verdú, M. M. Ugeda, I. Guillaumon, H. Suderow, J. I. Pascual, and N. Lorente, *Phys. Rev. Lett.* **120**, 167001 (2018).
- [17] K. Rossnagel, O. Seifarth, L. Kipp, M. Skibowski, D. Voß, P. Krüger, A. Mazur, and J. Pollmann, *Phys. Rev. B* **64**, 235119 (2001).
- [18] M. D. Johannes, I. I. Mazin, and C. A. Howells, *Phys. Rev. B* **73**, 205102 (2006).
- [19] T. Kiss, T. Yokoya, A. Chainani, S. Shin, T. Hanaguri, M. Nohara, and H. Takagi, *Nature Phys.* **3**, 720 (2007).
- [20] M. D. Johannes and I. I. Mazin, *Phys. Rev. B* **77**, 165135 (2008).
- [21] D. J. Rahn, S. Hellmann, M. Kalläne, C. Sohr, T. K. Kim, L. Kipp, and K. Rossnagel, *Phys. Rev. B* **85**, 224532 (2012).
- [22] C. D. Malliakas and M. G. Kanatzidis, *J. Am. Chem. Soc.* **135**, 1719 (2013).
- [23] J. Dai, E. Calleja, J. Alldredge, X. Zhu, L. Li, W. Lu, Y. Sun, T. Wolf, H. Berger, and K. McElroy, *Phys. Rev. B* **89**, 165140 (2014).
- [24] C. J. Arguello, S. P. Chockalingam, E. P. Rosenthal, L. Zhao, C. Gutiérrez, J. H. Kang, W. C. Chung, R. M. Fernandes, S. Jia, A. J. Millis, R. J. Cava, and A. N. Pasupathy, *Phys. Rev. B* **89**, 235115 (2014).
- [25] C. J. Arguello, E. P. Rosenthal, E. F. Andrade, W. Jin, P. C. Yeh, N. Zaki, S. Jia, R. J. Cava, R. M. Fernandes, A. J. Millis, T. Valla, R. M. Osgood, and A. N. Pasupathy, *Phys. Rev. Lett.* **114**, 037001 (2015).
- [26] F. Flicker and J. van Wezel, *Nature Comm.* **6**, 7034 (2015).
- [27] A. Soumyanarayanan, M. M. Yee, Y. He, J. van Wezel, D. J. Rahn, K. Rossnagel, E. W. Hudson, M. R. Norman, and J. E. Hoffman, *Proc. Natl. Acad. Sci.* **110**, 1623 (2013).
- [28] F. Weber, S. Rosenkranz, J.-P. Castellan, R. Osborn, R. Hott, R. Heid, K.-P. Bohnen, T. Egami, A. H. Said, and D. Reznik, *Phys. Rev. Lett.* **107**, 107403 (2011).
- [29] Areas with a Nb-centered CDW maxima (metal-centered, MC) do not appear in the STM images, as they have higher energy [47].
- [30] See supplemental material for more details of the theoretical considerations (mean-field description of the CDW, tight-binding model, coupling to the magnetic impurity, coupling to the CDW, numerical results) and additional experimental details (superconducting tip, numerical deconvolution of the spectra, identification of adsorption sites, determination of Fe atom position relative to CDW, additional spectra and maps).
- [31] In addition to the apparent height, both species also differ in the energies of their *d*-level resonances. We note that the apparent heights and *d*-level resonances are only slightly affected by the CDW. See SM [30] for more details.
- [32] H. F. Hess, R. B. Robinson, and J. V. Waszczak, *Phys. Rev. Lett.* **64**, 2711 (1990).
- [33] T. Yokoya, T. Kiss, A. Chainani, S. Shin, M. Nohara, and H. Takagi, *Science* **294**, 2518 (2001).
- [34] Y. Noat, T. Cren, F. Debontridder, D. Roditchev, W. Sacks, P. Toulemonde, and A. San Miguel, *Phys. Rev. B* **82**, 014531 (2010).
- [35] Y. Noat, J. A. Silva-Guillén, T. Cren, V. Cherkez, C. Brun, S. Pons, F. Debontridder, D. Roditchev, W. Sacks, L. Cario, P. Ordejón, A. García, and E. Canadell, *Phys. Rev. B* **92**, 134510 (2015).
- [36] J. G. Rodrigo and S. Vieira, *Physica C* **404**, 306 (2004).
- [37] E. Boaknin, M. A. Tanatar, J. Paglione, D. Hawthorn, F. Ronning, R. W. Hill, M. Sutherland, L. Taillefer, J. Sonier, S. M. Hayden, and J. W. Brill, *Phys. Rev. Lett.* **90**, 117003 (2003).
- [38] J. D. Fletcher, A. Carrington, P. Diener, P. Rodière, J. P. Brison, R. Prozorov, T. Olheiser, and R. W. Giannetta, *Phys. Rev. Lett.* **98**, 057003 (2007).
- [39] J. Senkpiel, C. Rubio-Verdu, M. Etzkorn, R. Drost, L. M. Schoop, S. Dambach, C. Padurariu, B. Kubala, J. Ankerhold, C. R. Ast, and K. Kern, arXiv:1803.08726v1.

- [40] The long-range oscillations are expected to have a period of half the Fermi wavelength in simple models of YSR states [3]. The Fermi surface of $2H$ -NbSe₂ consists of several sheets [17, 19, 21, 33] which can lead to a more complex structure in the long-range scattering pattern of the YSR wave functions.
- [41] K. J. Franke, G. Schulze, and J. I. Pascual, *Science* **332**, 940 (2011).
- [42] L. Farinacci, G. Ahmadi, G. Reecht, M. Ruby, N. Bogdanoff, O. Peters, B. W. Heinrich, F. von Oppen, and K. J. Franke, *Phys. Rev. Lett.* **121**, 196803 (2018).
- [43] L. Malavolti, M. Briganti, M. Hänze, G. Serrano, I. Cimatti, G. McMurtrie, E. Otero, P. Ohresser, F. Totti, M. Mannini, R. Sessoli, and S. Loth, *Nano Lett.* **18**, 7955 (2018).
- [44] X. Xi, Z. Wang, W. Zhao, J.-H. Park, K. T. Law, H. Berger, L. Forró, J. Shan, and K. F. Mak, *Nature Phys.* **12**, 139 (2016).
- [45] M. M. Ugeda, A. J. Bradley, Y. Zhang, S. Onishi, Y. Chen, W. Ruan, C. Ojeda-Aristizabal, H. Ryu, M. T. Edmonds, H.-Z. Tsai, A. Riss, S.-K. Mo, D. Lee, A. Zettl, Z. Hussain, Z.-X. Shen, and M. F. Crommie, *Nature Phys.* **12**, 92 (2016).
- [46] L. Bawden, S. P. Cooil, F. Mazzola, J. M. Riley, L. J. Collins-McIntyre, V. Sunko, K. W. B. Hunvik, M. Leandersson, C. M. Polley, T. Balasubramanian, T. K. Kim, M. Hoesch, J. W. Wells, G. Balakrishnan, M. S. Bahramy, and P. D. C. King, *Nature Comm.* **7**, 11711 (2016).
- [47] G. Gye, E. Oh, and H. W. Yeom, *Phys. Rev. Lett.* **122**, 016403 (2019).

SUPPLEMENTAL MATERIAL

THEORETICAL CONSIDERATIONS

Mean-field description of the CDW

We resort to a phenomenological mean-field description. We start with a generic Fröhlich-type Hamiltonian describing electrons coupled to phonons [1],

$$H = \sum_{\mathbf{k}} \epsilon_{\mathbf{k}} c_{\mathbf{k}}^{\dagger} c_{\mathbf{k}} + \sum_{\mathbf{q}} \omega_{\mathbf{q}} b_{\mathbf{q}}^{\dagger} b_{\mathbf{q}} + \sum_{\mathbf{k}, \mathbf{q}} g_{\mathbf{q}} (b_{\mathbf{q}} + b_{-\mathbf{q}}^{\dagger}) c_{\mathbf{k}+\mathbf{q}}^{\dagger} c_{\mathbf{k}}. \quad (\text{S1})$$

Here, $c_{\mathbf{k}}$ annihilates electrons with momentum \mathbf{k} and energy $\epsilon_{\mathbf{k}}$, $b_{\mathbf{q}}$ annihilates a phonon with wavevector \mathbf{q} and frequency $\omega_{\mathbf{q}}$, and $g_{\mathbf{q}}$ denotes the strength of the electron-phonon coupling. Within mean-field theory, we assume that certain phonon modes (denoted by \mathbf{Q}) go soft due to their coupling to the electronic system and develop a finite expectation value. Restricting to the lowest Fourier components and neglecting phonon dynamics beyond the static CDW distortions, we find the mean-field Hamiltonian

$$H = \sum_{\mathbf{k}} \epsilon_{\mathbf{k}} c_{\mathbf{k}}^{\dagger} c_{\mathbf{k}} + \sum_{\mathbf{k}} \sum_{\mathbf{Q}} g_{\mathbf{Q}} \langle b_{\mathbf{Q}} + b_{-\mathbf{Q}}^{\dagger} \rangle c_{\mathbf{k}+\mathbf{Q}}^{\dagger} c_{\mathbf{k}} \quad (\text{S2})$$

for the electronic degrees of freedom. Within this approach, the CDW acts on the electrons as a periodic potential $V_{\text{cdw}}(\mathbf{r})$. Indeed, the electron-phonon interaction term can also be expressed in real space as

$$H_{\text{el-ph}} = \int d\mathbf{r} V_{\text{cdw}}(\mathbf{r}) \psi^{\dagger}(\mathbf{r}) \psi(\mathbf{r}), \quad (\text{S3})$$

where

$$V_{\text{cdw}}(\mathbf{r}) = \sum_{\mathbf{Q}} e^{-i\mathbf{Q}\cdot\mathbf{r}} g_{\mathbf{Q}} \langle b_{\mathbf{Q}} + b_{-\mathbf{Q}}^{\dagger} \rangle. \quad (\text{S4})$$

To find the vectors \mathbf{Q} , consider a triangular lattice of Nb atoms with lattice vectors

$$\mathbf{a}_1 = a(1, 0), \quad (\text{S5})$$

$$\mathbf{a}_2 = a(1/2, \sqrt{3}/2) \quad (\text{S6})$$

and bond length $a = 3.445 \text{ \AA}$. The corresponding reciprocal lattice vectors \mathbf{b}_i satisfying $\mathbf{a}_i \cdot \mathbf{b}_j = 2\pi\delta_{ij}$ are

$$\mathbf{b}_1 = \frac{4\pi}{\sqrt{3}a}(\sqrt{3}/2, -1/2), \quad (\text{S7})$$

$$\mathbf{b}_2 = \frac{4\pi}{\sqrt{3}a}(0, 1). \quad (\text{S8})$$

The unit cell of the CDW has a linear dimension which is approximately three times larger than the unit cell of the atomic lattice, $\mathbf{a}^{\text{cdw}} \approx 3\mathbf{a}_i$ (for $i = 1, 2$). Correspondingly, the reciprocal lattice vectors of the CDW are approximately a factor of three smaller, $\mathbf{b}_i^{\text{cdw}} \approx \mathbf{b}_i/3$. Then, the first harmonics of the CDW have wavevectors

$$\mathbf{Q}_1 = q(1 - \delta)(\sqrt{3}/2, -1/2), \quad (\text{S9})$$

$$\mathbf{Q}_2 = q(1 - \delta)(0, 1), \quad (\text{S10})$$

$$\mathbf{Q}_3 = q(1 - \delta)(-\sqrt{3}/2, -1/2) = -(\mathbf{Q}_1 + \mathbf{Q}_2), \quad (\text{S11})$$

where $q = \frac{4\pi}{3\sqrt{3}a}$, and $\delta \ll 1$ accounts for the fact that the CDW is not exactly commensurate with the lattice.

Tight-binding model

To illustrate the effect of the CDW on the YSR state wave function, we perform model calculations within an effective tight-binding description. Specifically, we implement a model for the NbSe₂ band structure first introduced

	t_0	t_1	t_2	t_3	t_4	t_5
band 1	10.9	86.8	139.9	29.6	3.5	3.3
band 2	203.0	46.0	257.5	4.4	-15.0	6.0

Table S1. Values of the fitting parameters t_n in Eq. (S12) in meV.

in Ref. [2] and later used in Refs. [3–7]. The model uses that the relevant states near the Fermi energy have mostly Nb character and therefore focuses on one atomic d -orbital per niobium atom. (The model neglects an additional band centered at the Γ point which predominantly derives from Se orbitals and has strongly three-dimensional character [8].) Reducing the band-structure problem to the triangular Nb lattice makes it necessary to include hopping up to fifth nearest neighbors to reproduce the NbSe₂ band structure. The resulting band structure

$$E(\mathbf{k}) = t_0 + t_1(2 \cos \xi \cos \eta + \cos 2\xi) + t_2(2 \cos 3\xi \cos \eta + \cos 2\eta) + t_3(2 \cos 2\xi \cos 2\eta + \cos 4\xi) \\ + t_4(\cos \xi \cos 3\eta + \cos 5\xi \cos \eta + \cos 4\xi \cos 2\eta) + t_5(2 \cos 3\xi \cos 3\eta + \cos 6\xi) \quad (\text{S12})$$

is sixfold symmetric about the Γ point. Here, we defined $\xi = k_x/2$ and $\eta = \sqrt{3}k_y/2$. The hopping strengths t_n are used as fitting parameters to reproduce the NbSe₂ band structure. The values of the parameters t_n are given in Table S1 [6] for the two bands. The parameters for band 1 reproduce the inner cylindrical bands of NbSe₂, while the parameters for band 2 reproduce the outer bands. Figure S1a shows the Fermi surfaces of the two bands, with the Brillouin zone outlined in gray.

While this model accounts for the symmetries of the band structure and the approximate shapes of the Fermi surfaces, it is limited in other ways. To start with, the model neglects interlayer coupling which, however, is expected to be weak compared to the intralayer couplings. In this approximation, it suffices to consider a single (tri)layer of 2H-NbSe₂, consisting of a Nb layer sandwiched between two Se layers with equal orientations of the triangles.

The model also ignores effects of spin orbit coupling which are known to be substantial [9]. A single (tri)layer of 2H-NbSe₂, does not have an inversion center, so that spin-orbit coupling leads to spin-split bands. This can be roughly thought of by analogy with graphene. When projected into a plane, a 2H-NbSe₂ trilayer has a honeycomb lattice structure with the Nb and Se atoms located on the A and B sublattices, respectively. There are three important modifications relative to graphene: (i) The sublattice asymmetry breaks inversion symmetry and opens gaps at the K points. (ii) By stoichiometry, the Fermi energy is in the valence band such that there are Fermi pockets around the K points. It turns out that there is an additional Fermi pocket around the Γ point. (iii) There is substantial spin-orbit coupling. By reflection symmetry about the Nb layer, the electric fields underlying the spin-orbit coupling point in plane as do the momenta. As a result, the spin-orbit field is pointing perpendicular to the plane and in opposite directions at the two K points, as enforced by time-reversal symmetry. This Ising spin-orbit coupling polarizes the spins at the K and K' points in opposite directions, splitting the corresponding Fermi surfaces into separate spin-up and spin-down Fermi surfaces.

The elementary layer of bulk 2H-NbSe₂ consists of two trilayers with the orientations of the Se lattices rotated by 180 degrees with respect to one another. Neglecting interlayer coupling, the band structure of the second trilayer is identical to the first (but differs in the spin assignments). Thus, the bulk crystal has twofold degenerate bands, consistent with the fact that it has an inversion center located between the trilayers.

It is natural to assume that the adatom predominantly couples to one of the trilayers. In this sense, the band structure in Eq. (S12) should be a good starting point. However, while incorporating the correct symmetries, the model does not capture other aspects of the band structure such as the spin textures of the Fermi surface which may be relevant for some aspects of the YSR physics.

To account for superconductivity, we incorporate this tight-binding Hamiltonian into a Bogoliubov-deGennes Hamiltonian with conventional s -wave pairing. We choose the pairing strength to be $\Delta = 1\text{meV}$. In experiment, one finds multiple coherence peaks for 2H-NbSe₂, which has been interpreted in terms of multiband or anisotropic superconductivity. Our modeling does not account for this effect. However, the chosen value for Δ falls into the range of the peak distribution ($0.7 - 1.4\text{meV}$) found in experiment.

Coupling to the magnetic impurity

Following Ref. [7], we couple a magnetic impurity as a classical spin S through the exchange interaction $JS\sigma_z/2$ with accompanying potential scattering K . For simplicity, we place the impurity on one of the sites of the triangular

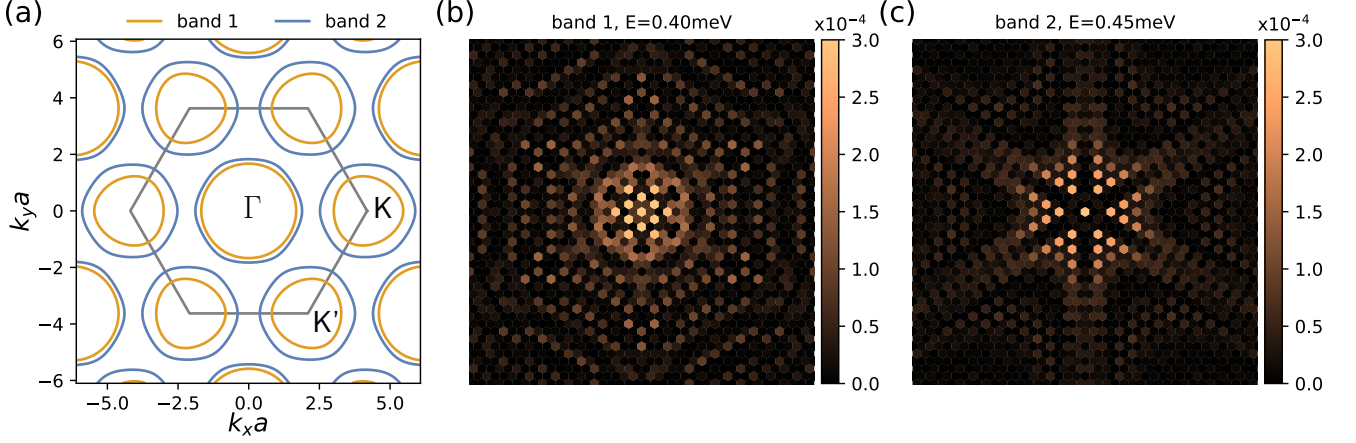


Figure S1. (a) Fermi surfaces of bands 1 and 2 (see Eq. (S12) and Table S1). (b)-(c), Electronic probability density $|u(\mathbf{r})|^2$ of the YSR state in the absence of the CDW for $JS/2 = 120$ meV, $K = 0$ and a lattice of size 504×504 with periodic boundary conditions for band 1 (b) and band 2 (c). The region shown includes 40×40 lattice spacings.

lattice.[?]] Thus, we model the coupling of the adatom to the substrate as

$$H_{\text{ad}} = -\frac{JS}{2}(c_{\mathbf{r}_0\uparrow}^\dagger c_{\mathbf{r}_0\uparrow} - c_{\mathbf{r}_0\downarrow}^\dagger c_{\mathbf{r}_0\downarrow}) + K(c_{\mathbf{r}_0\uparrow}^\dagger c_{\mathbf{r}_0\uparrow} + c_{\mathbf{r}_0\downarrow}^\dagger c_{\mathbf{r}_0\downarrow}). \quad (\text{S13})$$

Here, $c_{\mathbf{r}_0\sigma}$ annihilates an electron with spin σ at the adatom position \mathbf{r}_0 .

This couples the impurity to only one of the two Fermi surfaces (band 1 or band 2), leading to one YSR state per band. Figures S1b and c show the probability densities of the YSR states for band 1 and 2 respectively, for a specific choice of parameters. The spatial distribution of the probability density is sixfold symmetric in both cases. Due to the more isotropic character of band 1, the corresponding YSR state is also more spatially isotropic than its band 2 counterpart, which exhibits a more pronounced anisotropy.

Within an underlying Anderson model, we should couple the impurity to both bands. The exchange coupling and potential scattering do not conserve the band index, but can also scatter electrons between bands. Under rather general assumptions, this still leads only to a single pair of YSR states [10, 11]. While we show results for the YSR states when coupling only to band 1 or only to band 2, we emphasize that a more accurate treatment of the two-band substrate would result only in a single pair of YSR states. The two sets of YSR states should merely be viewed as illustration of the variability of the YSR states with the band structure model.

This coupling also neglects the d -orbital physics of the impurity beyond the fact that it gives rise to a magnetic moment. This d -level physics has been elucidated for the case of a half-filled d shell in the high-spin configuration [12]. Here, we are dealing with Fe adatoms for which the d -orbital physics is more involved. A detailed understanding of this physics is an interesting problem for future work and beyond the scope of this paper.

Coupling to the CDW

As explained above, the effect of the CDW on the electrons of the substrate can be described through a periodic potential. Within the tight-binding model, we include the CDW as a modulation of the on-site potential,

$$H_{\text{cdw}} = \sum_{\mathbf{r}, \sigma} c_{\mathbf{r}\sigma}^\dagger V(\mathbf{r}) c_{\mathbf{r}\sigma}, \quad (\text{S14})$$

where the sum runs over the lattice sites of the triangular Nb lattice. The CDW potential $V(\mathbf{r})$ is constructed from the main Fourier components of the CDW [see Eq. (S11)],

$$V(\mathbf{r}) = V_0 [\cos(\mathbf{Q}_1 \cdot \mathbf{r} + \phi_1) + \cos(\mathbf{Q}_2 \cdot \mathbf{r} + \phi_2) + \cos(\mathbf{Q}_3 \cdot \mathbf{r} + \phi_3)], \quad (\text{S15})$$

where V_0 denotes the amplitude of the CDW potential. Except for $\phi_1 = \phi_2 = \phi_3$ and similar fine-tuned cases, typical choices of the phases ϕ_i yield CDW potentials with the desired symmetry and shape, exhibiting an absolute maximum, an absolute minimum, and a local minimum/saddle point. For definiteness, we choose $\phi_1 = \phi_2 = 0$.

Due to the small deviations from commensurability, the CDW shifts slowly as a function of position relative to the underlying atomic lattice. On the scale of the YSR states, these shifts can be considered constant so that the CDW potential can be written as

$$V(\mathbf{r}) = V_0 \left[2 \cos \left(\sqrt{3} \frac{q}{2} (x - x_0) \right) \cos \left(\frac{q}{2} (y - y_0) \right) + \cos (q(y - y_0) + \phi_3) \right], \quad (\text{S16})$$

where $q = 4\pi/3\sqrt{3}$. The offsets x_0 and y_0 originate from the deviation δ from commensurability, and describe the local shift of the CDW relative to the atomic lattice. In the experiment, the measured maxima of the CDW correspond to regions where the lattice deformation compresses the ions, creating an attractive potential for the electrons. For this reason we choose the potential $V(\mathbf{r})$ to have minima where the measured tunneling DOS has maxima, *i.e.*, position I of the adatom corresponds to a minimum of $V(\mathbf{r})$ and position III corresponds to a maximum. In principle, the CDW may also modulate the hopping parameters of the tight-binding model, but the effective long-range hopping processes of the model make this cumbersome to include.

Numerical results

Within this model, we can study how the wavefunction and the energy of YSR states depend on the adatom position relative to the CDW. As discussed above, the model cannot reproduce the experimental results quantitatively as it neglects various relevant effects. Nevertheless, the model is expected to capture the symmetries of the YSR wavefunctions and to provide insights into the qualitative dependence of the YSR energy on the adsorption site relative to the CDW.

Figure S2 shows the probability density of the YSR wavefunction for the six different positions of the adatom relative to the CDW, as discussed in the main text. The results are obtained for the parameters of band 2. The adatoms in positions I and III are at the minimum and the maximum of the CDW, respectively, *i.e.*, at points with a threefold symmetric environment. Consequently, the corresponding density plots (Fig. S2a and c) present threefold symmetry. Positions II, IV, and V exhibit reflection symmetry about an axis that passes through the adatom. For the corresponding plots shown in Fig. S2b, d, and e, this axis is aligned along the vertical direction. Finally, position VI has no symmetries with respect to the CDW and consequently, the state shown in Fig. S2f also exhibits no symmetries. Interestingly, the YSR state seems to retain the original sixfold symmetry (without CDW) to some degree (compare with Fig. S1c).

Figure S3 shows equivalent plots for band 1. This figure complements the probability densities shown in the main paper with results for additional adsorption sites. Due to the more isotropic character of band 1, the threefold symmetry is less pronounced in these plots. Remarkably, position VI (Fig. S3f) does not preserve any of the original sixfold symmetry in the vicinity of the adatom. More generally, a comparison between Figs. S2 and S3 shows that the detailed YSR wavefunctions depend quite sensitively on the band structure parameters.

Finally, we discuss the correlation of the energy of the YSR state with the modulation of the local density of states by the CDW, as shown in Fig. 4 in the main text. Within a simple model of a classical magnetic impurity, the energy of YSR states depends on the strength of the exchange coupling as measured by the dimensionless parameter $\alpha = \pi\nu_0 JS/2$, where ν_0 is the density of states, J the exchange coupling, and S the impurity spin. Thus, one indeed expects the energy of the YSR state to depend on the density of states ν_0 . The direction of the energy shift depends on whether the impurity is weakly or strongly coupled, corresponding to unscreened or (partially) screened impurity spins, respectively. The energy of the positive-energy YSR state decreases (increases) with the density of states, depending on whether the impurity spin is unscreened (screened). Variations in the local density of states due to the CDW should thus be reflected in the energy of the YSR states. Within this picture, the observed correlations suggest that in our experiment the impurity is in the strong-coupling limit.

This interpretation is consistent with our theoretical results. However, we find that in general the CDW affects the energy of the YSR state through two mechanisms. In addition to the density of states effect, the CDW potential also has a second effect which can be roughly rationalized as the CDW affecting the strength of potential scattering from the impurity and thereby shifting the YSR energy. Including potential scattering within the simple model, the energy of a YSR state is given by [13–15]

$$E = \pm \Delta \frac{1 - \alpha^2 + \beta^2}{\sqrt{4\alpha^2 + (1 - \alpha^2 + \beta^2)^2}}, \quad (\text{S17})$$

where $\beta = \pi\nu_0 K$ is a dimensionless measure of the strength of the potential scattering K . The transition between weak and strong coupling takes place at $\alpha^2 = 1 + \beta^2$ where the energy of the YSR state passes through zero. Roughly,

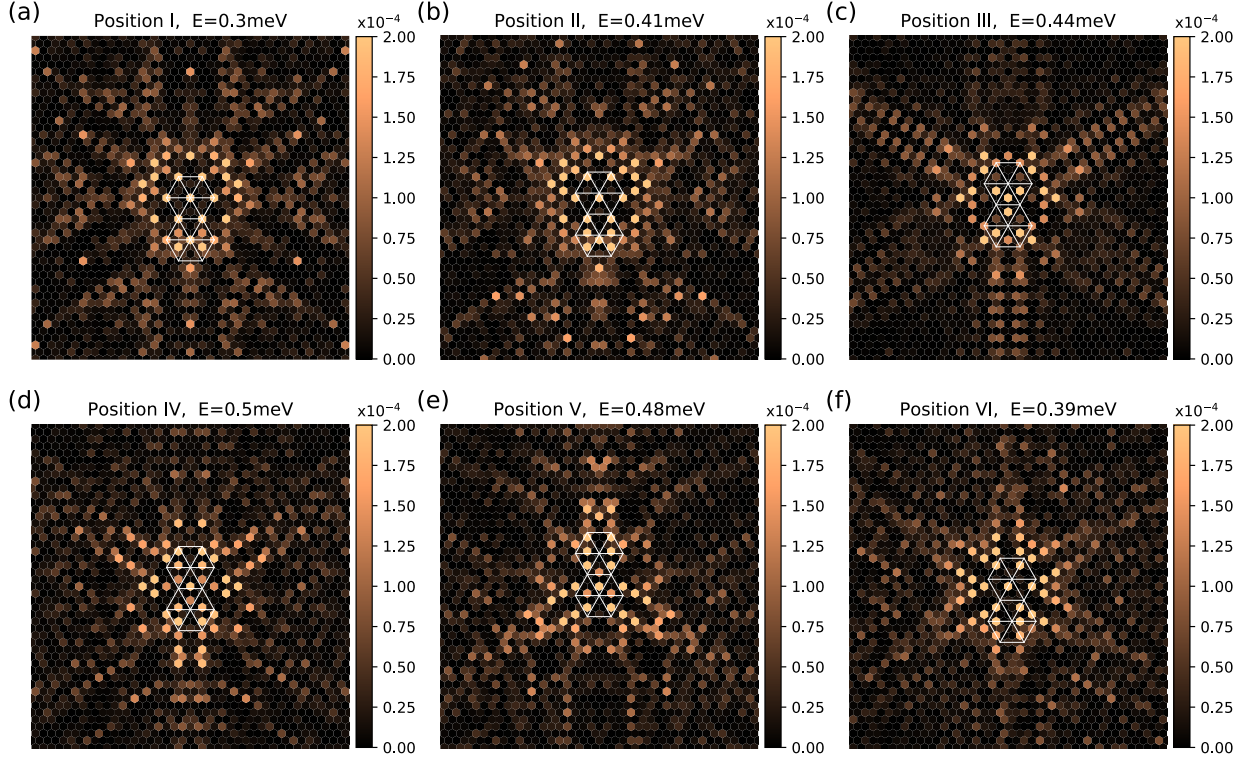


Figure S2. Electronic probability density $|u(\mathbf{r})|^2$ of the YSR state in the presence of the CDW potential for band 2 and for adatoms located at positions equivalent to those studied experimentally as presented in the main text. For all plots, the parameters are $JS/2 = 120\text{meV}$, $K = 0$, $V_0 = -30\text{meV}$, $\phi = \pi/3$ and a lattice of size 504×504 with periodic boundary conditions. The region shown includes 40×40 lattice spacings. The white lines outline the CDW, with crossing lines indicating a maximum of the CDW.

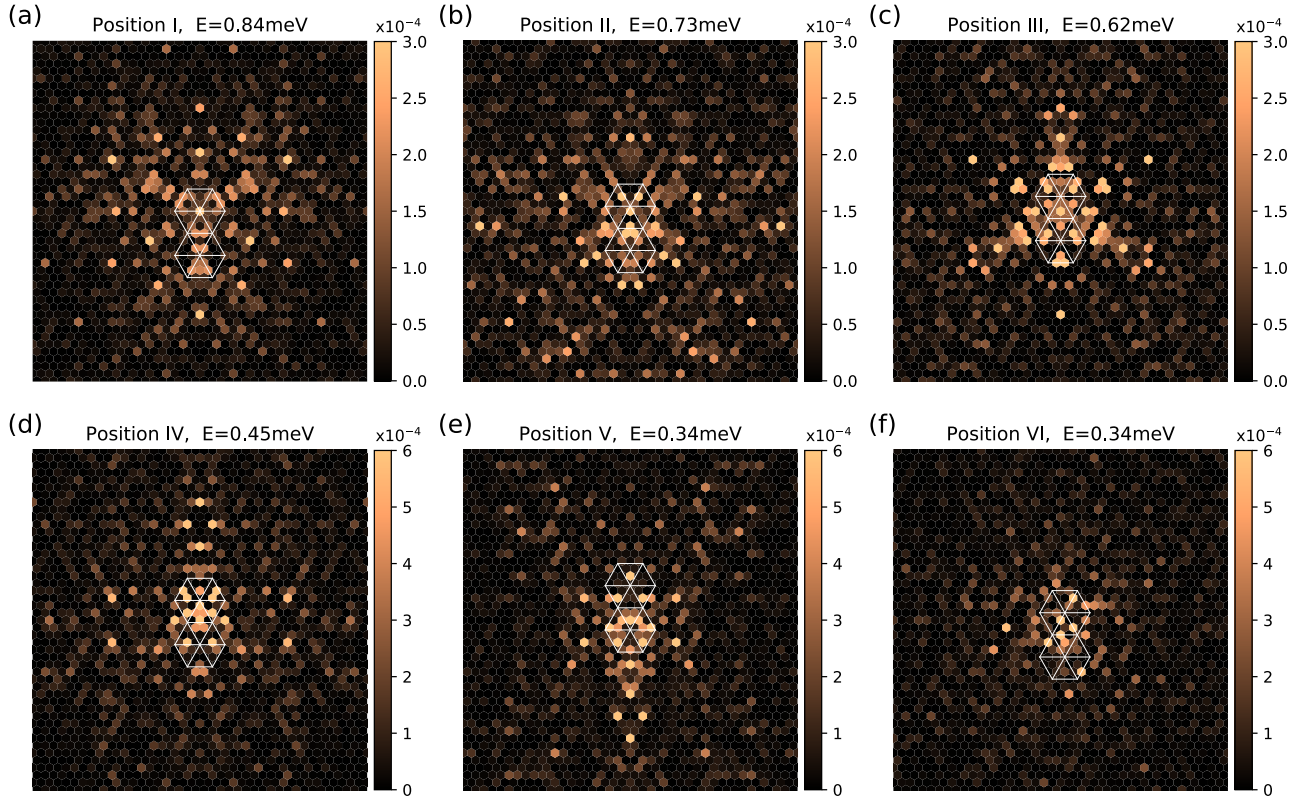


Figure S3. Analogous plots to those in Fig. S2 for band 1. Parameters: $JS/2 = 120\text{meV}$, $K = 0$, $V_0 = -30\text{meV}$, $\phi = \pi/3$ and a lattice of size 504×504 with periodic boundary conditions. The region shown includes 40×40 lattice spacings.

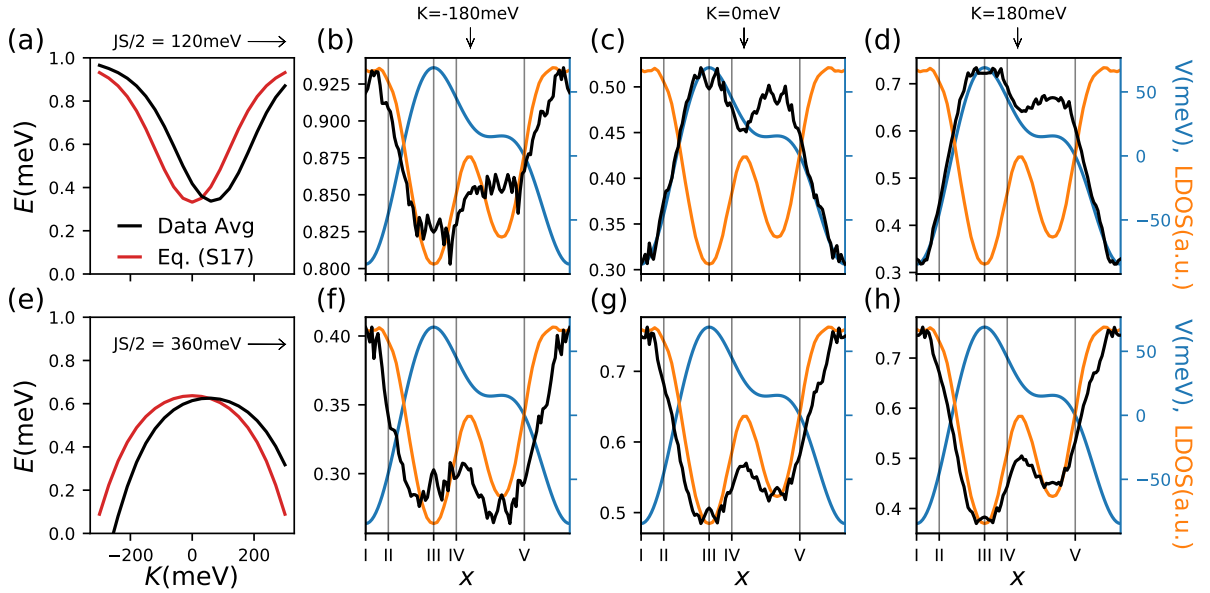


Figure S4. Tight-binding calculations for the energy of the YSR state as a function of the position of the adatom relative to the CDW, for various potential scattering strengths K . Panels (a) and (e) show, for the weakly and strongly coupled regimes, respectively, the energy of the YSR state E vs. K , as obtained by averaging over different positions of the adatom relative to the CDW (black) and as given by Eq. (S17) for an appropriately chosen ν_0 (red). Panels (b)-(d) show E vs. adatom position in the weakly coupled regime for three different K . The plots show the local density of states LDOS (orange) to anticorrelate with the CDW potential V (blue). Panels (c) and (d) show the energy to correlate with the CDW potential V (anticorrelate with the LDOS). For $K = -180$ meV shown in panel (b) the correlation inverts due to the shift of K to $K + V(\mathbf{r}_0)$ (see text). Panels (f)-(h) show equivalent plots for the strongly coupled regime, where the effect of K is less relevant. The energy E is correlated with the LDOS as expected from Eq. (S17). For all plots, the parameters are $V_0 = -30$ meV, $\phi = \pi/3$, and a lattice size of 750×750 .

the CDW potential V seems to shift K to $K + V(\mathbf{r}_0)$, where \mathbf{r}_0 denotes the adsorption site of the impurity. For comparison with experiment, it is important to note that an increase in the CDW potential *decreases* the density of states. This can be seen in e.g. Fig. S4(g), which shows numerical results for the local density of states (orange) in the presence of the CDW potential (blue) as obtained from a straight-forward band structure calculation. Thus, the experiment implies an anticorrelation between the CDW potential V and the energy of the YSR states.

To illustrate these two effects of the CDW potential, we calculate the YRS energy for different adatom positions and various values of K . Consider first the results for weak coupling. We find that depending on the strength K of potential scattering, the CDW potential is correlated or anticorrelated with the energy of the YSR state. For $K = 180$ meV and $K = 0$, the energy is correlated with the CDW potential, see Fig. S4(c) and (d). In contrast, we find anticorrelations for $K = -180$ meV, see Fig. S4(b). The correlations observed at $K = 0$ are consistent with the effect of the CDW potential on the density of states. At this K , the energy shift of the YSR states due to the change in potential scattering, K to $K + V(\mathbf{r}_0)$, is weak since the energy of the YSR states is only weakly dependent on K near the minimum at $K = 0$. This is illustrated in Fig. S4(a) which shows the dependence of the energy of the YSR state on K in the weak-coupling regime. Specifically, the black curve averages data for the energy of the YSR state over different adatom positions. The red curve corresponds to Eq. (S17) with the same values for JS and K and an appropriately chosen density of states ν_0 . Both curves exhibit similar ‘parabolic’ behaviors.

For the strongly coupled regime, we find anticorrelations between the CDW potential and the energy of the YSR state – and thus correlations between the local density of states and the YSR energy – for all values of K , see Fig. S4(f), (g), and (h). These correlations between the density of states and the YSR energy are consistent with experiment. To start with, the anticorrelations at $K = 0$ are consistent with the expected density of states effect according to Eq. (S17). For strong coupling, the dependence of the YSR energy on K is generally weaker compared to the weak coupling case, see Fig. S4(e). For this reason, the shift of K by the CDW potential no longer overcomes the DOS effect. Thus, unless the impurity is a surprisingly strong potential scatterer, we conclude that in experiment the impurity is in the strong coupling limit.

EXPERIMENTAL DETAILS

Superconducting tip

In order to increase the energy resolution beyond the Fermi-Dirac limit, all measurements presented in the manuscript were performed using a superconducting Pb tip fabricated by indenting a W tip into a clean Pb(111) surface until the tip exhibits a bulk-like superconducting gap. Details of the preparation procedure for tip and sample are described in [16]. The tunneling current is proportional to the convolution of the DOS of the sample ρ_s and tip ρ_t and can be expressed as [17]:

$$I(V) \propto \int_{-\infty}^{+\infty} dE \rho_t(E - eV, T) \rho_s(E, T) [f(E - eV, T) - f(E, T)] |M_{\mu, \nu}|^2. \quad (\text{S18})$$

Here, $f(E, T)$ is the Fermi-Dirac-distribution function accounting for the thermal occupation of the states in the tip and the sample, and $|M_{\mu, \nu}|$ is the tunneling matrix element between the initial state μ and final state ν .

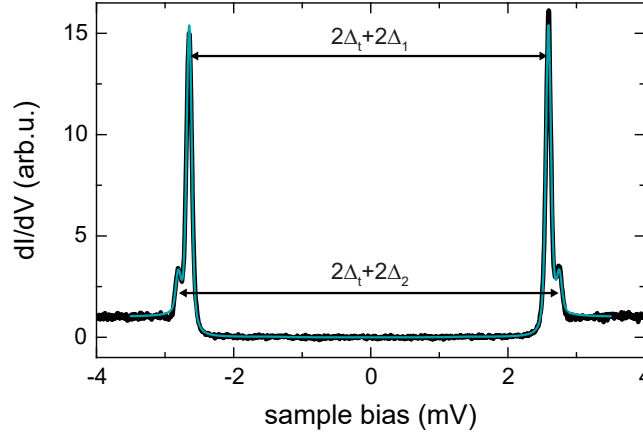


Figure S5. Spectrum taken with a Pb tip on a bare Pb(111) crystal with a set point 4 mV, 200 pA at $T = 1.1$ K. The fit (shown in green) is performed as described in [18].

This leads to the differential conductance:

$$\frac{\partial I}{\partial V} \propto \int_{-\infty}^{+\infty} dE \frac{\partial \rho_t(E - eV)}{\partial V} \rho_s(E, T) [f(E - eV, T) - f(E, T)] + \int_{-\infty}^{+\infty} dE \rho_t(E - eV) \rho_s(E, T) \frac{\partial f(E - eV, T)}{\partial V}. \quad (\text{S19})$$

Before investigating the NbSe₂ sample, the tip was characterized on a clean Pb(111) sample. A spectrum taken on bare Pb(111) after preparation of the Pb tip is shown in Fig. S5. The two superconducting energy gaps of the substrate are well resolved [18]. The Pb tip was characterized by the fit procedure described in detail in [18] where a BCS like DOS is assumed for the tip:

$$\rho_t(E) = \text{sgn}(E) \Re \left(\frac{E - i\Gamma}{\sqrt{(E - i\Gamma)^2 + \Delta_t^2}} \right). \quad (\text{S20})$$

From this fitting procedure we determine the values for the superconducting energy gap Δ_t and the depairing factor Γ of the tip. The size of the energy gap $\Delta_t \approx 1.35$ meV does not vary for bulk-like tips, whereas the depairing factor was found to vary between $\Gamma \approx 10$ -20 μ eV for different tips.

Numerical deconvolution of the dI/dV spectra

In order to find the exact position of the YSR energies on the NbSe₂ sample, all data was numerically deconvolved as described in the following (similar to the procedure described in [19]). Equation (S19) can be discretized into matrix

form and then reads:

$$\frac{\partial \vec{I}}{\partial V}(V) \propto \mathbf{K}(E, V, T) \vec{\rho}_s(E). \quad (\text{S21})$$

The vector on the left hand side contains the differential conductance data, $\vec{\rho}_s(E)$ is the DOS of the sample. The matrix \mathbf{K} can be determined by comparing Eq. (S19) and Eq. (S21) to

$$\mathbf{K}_{ij}(E_j, V_i, T) = dE \frac{\partial \rho_t(E_j - eV_i)}{\partial V} [f(E_j - eV_i, T) - f(E_j, T)] + dE \rho_t(E_j - eV_i) \frac{\partial f(E_j - eV_i, T)}{\partial V}. \quad (\text{S22})$$

Thus, with the knowledge of the depairing factor and the energy gap of the tip, $\rho_s(E)$ can be calculated by finding the pseudoinverse of \mathbf{K} . In order to assure that the tip properties did not change during sample exchange from Pb to NbSe₂, we checked the accurateness of the tip's energy gap by deconvolution and recalculation of spectra on several Fe adatoms. If an inaccurate value of the energy gap is assumed for the tip, the energies of the thermally excited YSR resonances are found in a wrong position in the recalculated trace. Before deconvolving all spectra are normalized and smoothed using a Savitzky-Golay filter. Deconvolved spectra of atoms I-VI (*cf.* Fig. 2 in the main text) are shown in Fig. S6.

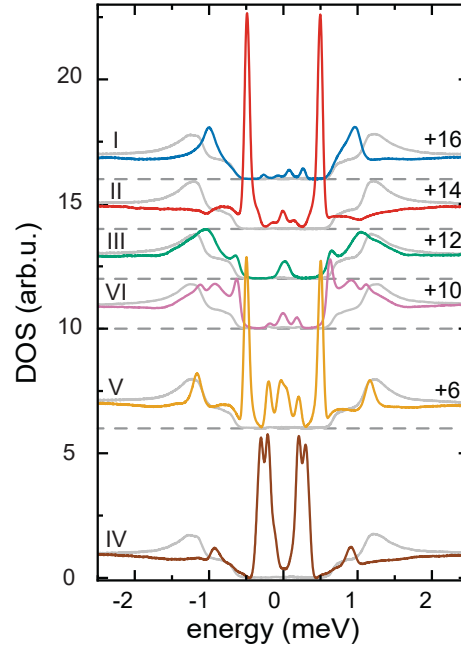


Figure S6. Deconvolved data of atom I-VI (substrate data is shown in grey). Offsets are indicated by the numbers on the right of each trace.

Identification of adsorption sites

A dilute coverage of Fe atoms (≈ 50 atoms/ $(100 \times 100 \text{ nm}^2)$) was deposited by evaporation on the NbSe₂ sample in the STM at temperatures below 12 K and a base pressure of $1 \cdot 10^{-10}$ mbar. Two distinct apparent heights of the Fe atoms are observed (Fig. S7 and Fig. 1 e,f in the main text). Furthermore, the two adatom types differ in the *d*-level resonances (see blue and orange data in Fig. S8a). Here, only minor differences arise within different atoms of one species.

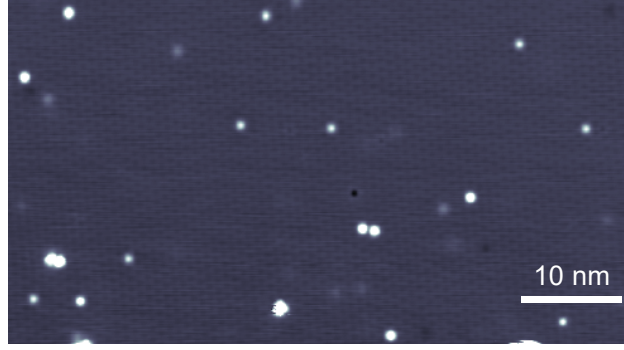


Figure S7. Overview image of the NbSe₂ surface after deposition of Fe adatoms (set point: 500 mV, 80 pA).

To identify the precise adsorption site of the two species, we recorded atomic-resolution images as shown in Fig. S8(b,c). With the atomic lattice superposed on the STM images we find that all Fe atoms reside in hollow sites of the terminating Se layer. The Fe atoms with large apparent height solely occupy hollow sites, where the neighboring Se atoms form a triangle pointing in one direction, while the atoms with low apparent height are enclosed by a Se triangle rotated by 180°. Inspection of the atomic structure of NbSe₂ shows that there are two distinct hollow sites which differ by the presence or absence of a Nb atom beneath (metal-centered, MC, or hollow-centered, HC).

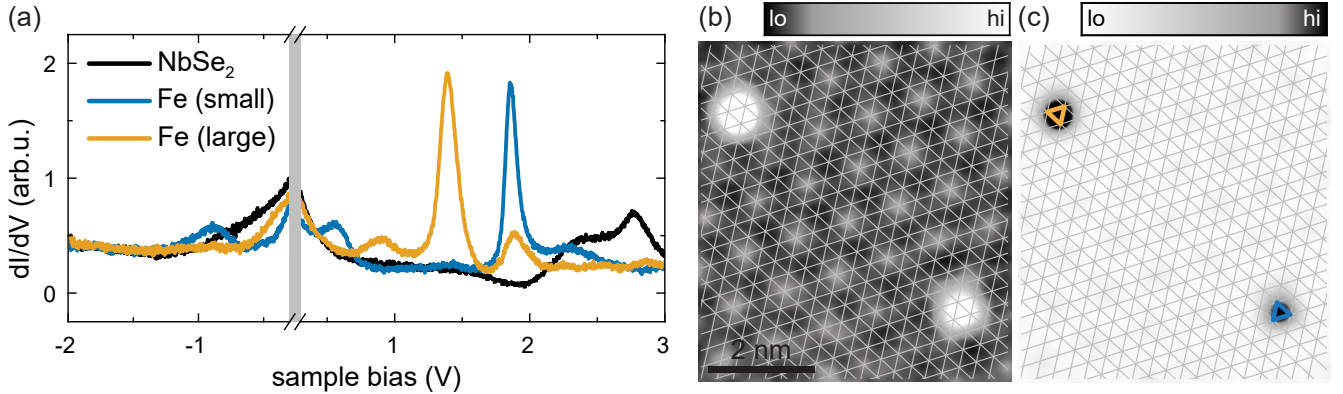


Figure S8. (a) Constant-current ($I = 100$ pA) spectra of NbSe₂ (black) and on Fe adatoms in different hollow site (blue, orange) as shown in (b,c). (b) Atomic-resolution STM image showing one adatom of each species (set point: 4 mV, 200 pA). The atomic lattice of the top Se layer is overlaid in grey. (c) The same topography and atomic lattice as shown in (a) with an inverted color code such that only the center of the atoms is visible. The orange and blue triangles point out the two different adsorption sites.

An unambiguous identification of the two hollow sites is possible by comparison to the location of the CDW. As discussed in the main text (Fig. 1a-d), the CDW maxima and minima can coincide with hollow sites (HC) or with a Se atom (chalcogenide-centered, CC), but are never located on the Nb sites (MC) [20]. As illustrated in Fig. S9a, b, Fe atoms with small apparent height can be found exactly in the minimum and maximum of the CDW. Hence, this species is assigned to adsorption in the HC position. Consequently, atoms with large apparent height are adsorbed in the MC sites.

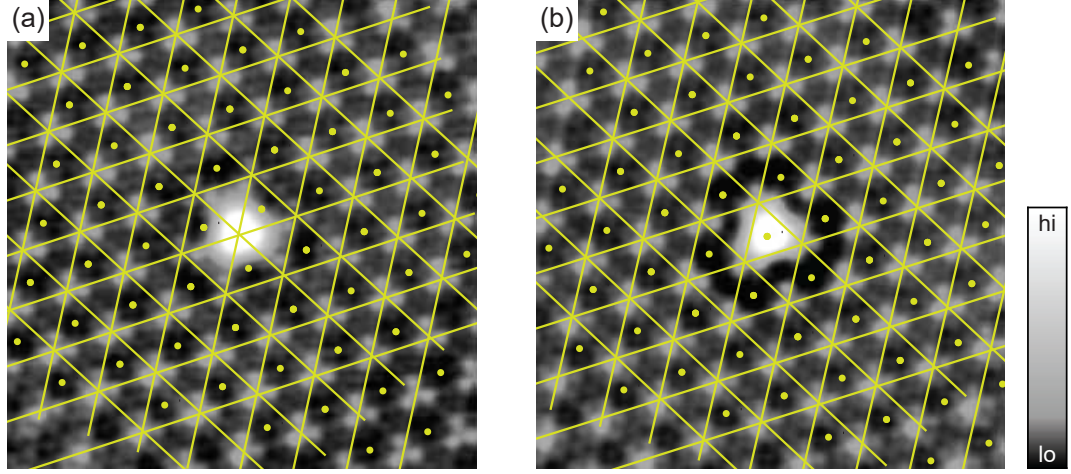


Figure S9. Atomic-resolution STM images of two adatoms with small apparent height, located on the maximum (a) and minimum (b) of the CDW (set point: 4 mV, 200 pA, $8 \times 8 \text{ nm}^2$). The intersections of the yellow grid correspond to maxima, the dots to the minima of the CDW.

Determination of Fe-atom adsorption sites relative to the CDW

The adsorption site of Fe atoms relative to the CDW was determined for a set of approximately 90 atoms (used for the data compilation in Fig. 4 of the main manuscript). The center of the Fe atoms as well as the location of the CDW can be determined from the STM images (see superposed CDW grid on the STM topographies in Fig. S10). The error in placing the CDW grids is estimated as $\delta x = \pm 0.05 a_{\text{cdw}}$, which accounts for the inaccuracy in placing the CDW grid, possible drift effects and for the inaccuracy in finding the center of the atom.

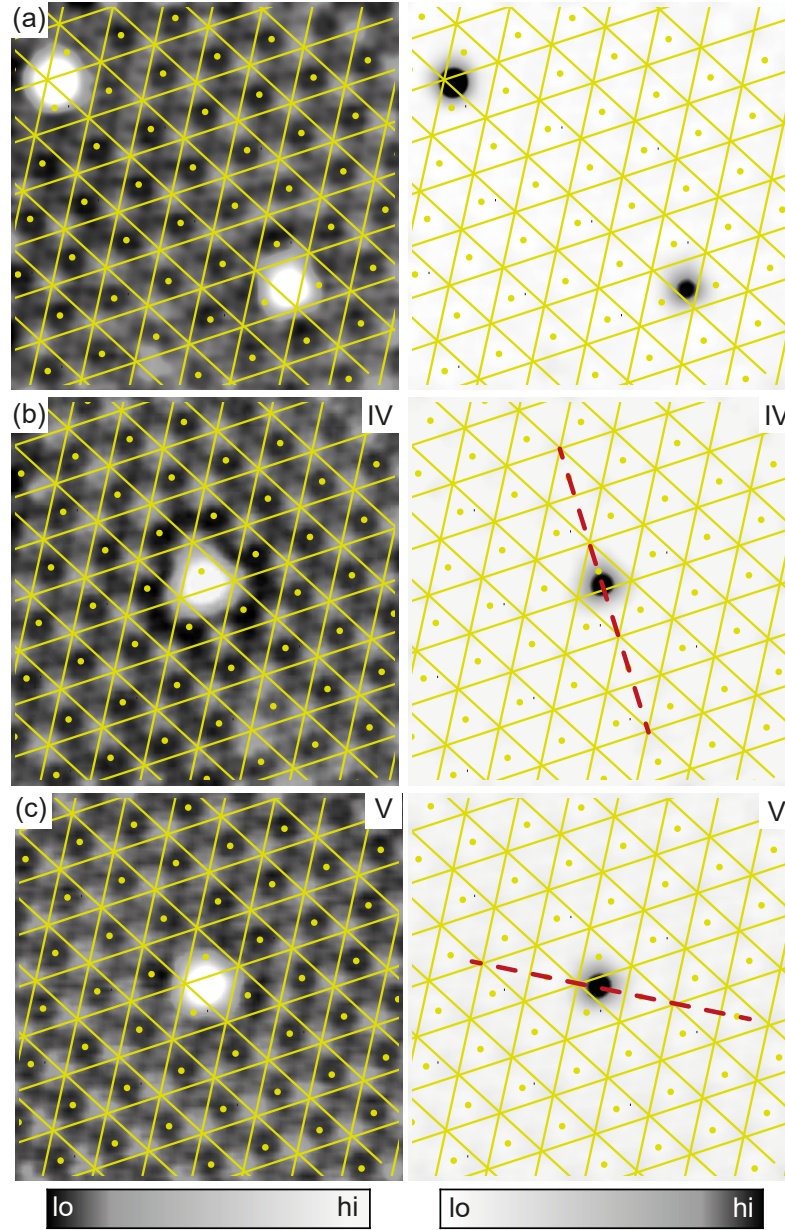


Figure S10. (a-c) The left panels show atomic resolution topographies overlaid with the CDW lattice (set point: 4 mV, 200 pA). The intersections of the yellow grid correspond to maxima of the CDW, the dots correspond to minima. In the right panel the center of the atoms can be identified (same images as in the left panel with reversed color code). (b) and (c) show atoms IV and V of the main manuscript. Red dashed lines in (b) and (c) indicate the symmetry axis (*cf.* Fig. 3 in the main text).

Pinning of the CDW

It has been shown that the CDW can be pinned by crystal defects [21–25]. Therefore, the phase of the CDW is dictated by the complex interplay of lattice defects and long-range order of the CDW. One such example of a local modification of the CDW in the presence of a defect can be seen in Fig. S11a in the bottom left, where the CC structure of the CDW is pinned around a defect (visible as depression). Hence, one may argue that the Fe atoms can affect the CDW. However, a pinning of the CDW by the adatoms is not observed in the experiment. The adatoms seem not to favor a specific CDW domain as can be seen in Fig. S11a and b. Here, pure HC and CC domains are marked. The adatoms are located in the smooth transition region.

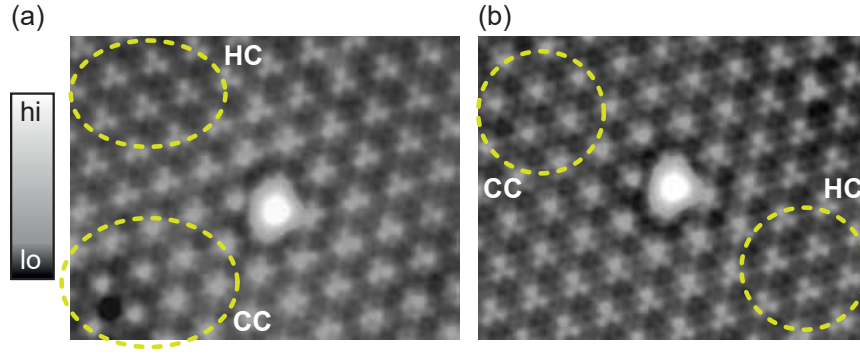


Figure S11. (a,b) Constant-current STM images ($9 \times 7 \text{ nm}^2$) of two HC adatoms (set point: 4 mV, 200 pA). A stretched color code is used to resolve the atomic corrugation. Dashed circles indicate pure HC and CC domains. In the bottom left of (a) there is a defect pinning the CC structure.

Spatial variation of dI/dV spectra

Figure S12 shows dI/dV spectra taken on and in close vicinity of atoms I-VI of the main text. The intensity of the resonances varies strongly with the precise location. This gives rise to the distinct dI/dV patterns around the atoms as shown in Fig. 3 of the main text. Here, we comment on the need of a very careful examination of the spectra. Some of the resonances are accompanied by a negative value of the differential conductance (NDC) at their high-bias flank. The NDC results from the convolution of YSR states with the tip DOS and can lead to a strong suppression of conductance. In an extreme case, an additional (weak) YSR resonance may be hidden in this part of the spectrum. Examples, where YSR resonances are suppressed below zero are shown by arrows for atom IV, V and VI in Fig. S12. The local variation of the NDC also affects the spatial appearance of the YSR states in the dI/dV maps as is discussed in the following section.

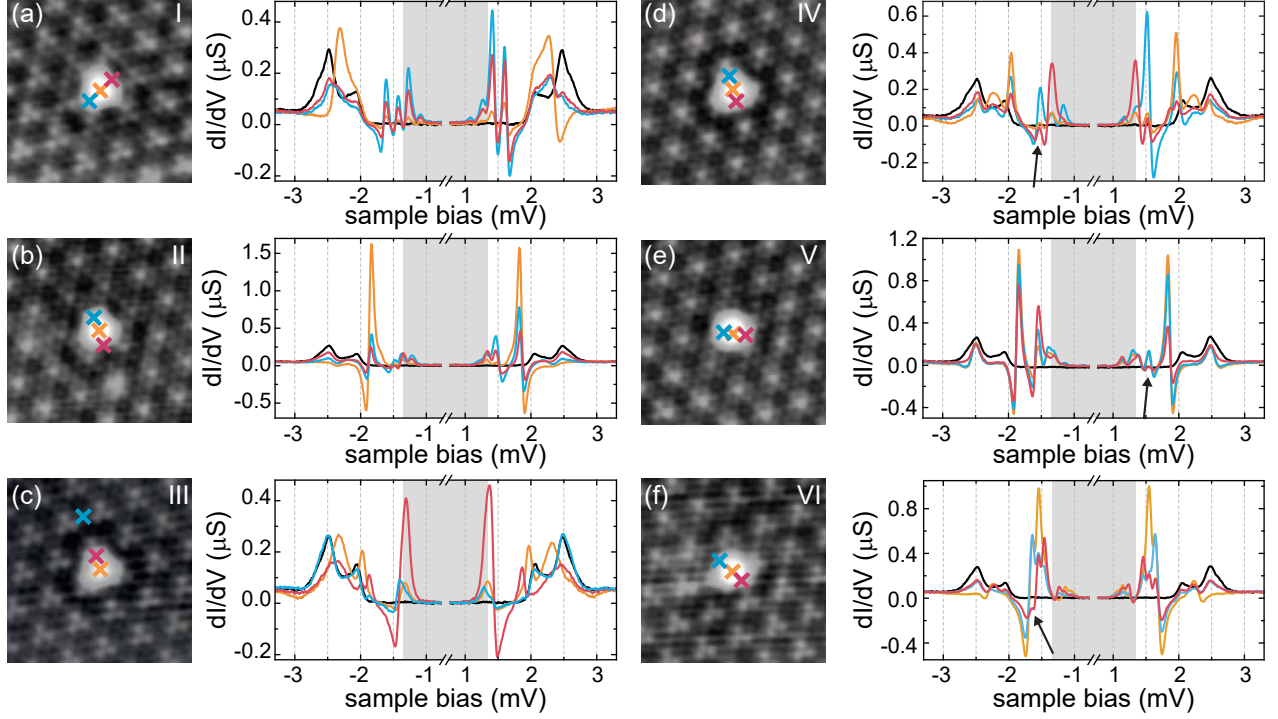


Figure S12. (a-f) Topography (left) and dI/dV spectra (right) taken on and in close vicinity of atoms I-VI of the main text. Colored crosses indicate the location of the spectra (set point: 4 mV, 200 pA). Corresponding substrate data are shown in black for each atom. Black arrows highlight YSR states that are strongly affected by the NDC due to a close-by YSR resonance.

Additional dI/dV maps of YSR resonances (both bias polarities and thermal excitations)

Figure S13 shows the complete set of the dI/dV maps of atoms I-VI (the positive bias voltage was presented in the main manuscript). dI/dV maps at negative bias polarity are depicted in the lower two rows. Opposite bias polarities image the $|u|^2$ and $|v|^2$ components of the YSR states, respectively [15].

As expected, the $|u|^2$ and $|v|^2$ components lead to distinct scattering patterns. As discussed above, the convolution of tip and sample DOS may lead to distortions of the intensity of individual YSR states, culminating in their suppression in the NDC region of a nearby state. Consequently, also the dI/dV maps at the energy of a specific YSR state may be affected by a close-lying YSR state.

In particular, the $\pm\beta$ -states of atom II, IV and V are affected by the NDC of the α -resonances, which are close in energy (Fig. S13). One trick to determine and eliminate the effect of NDC is to investigate the dI/dV maps of thermally excited YSR states. Thermal excitation of quasiparticles leads to additional resonances within the energy gap of the tip (*cf.* grey shaded area in Fig. 2 in the main text). Whereas the original resonances are found at a bias of $eV_{\pm\alpha,\pm\beta} = \pm|\Delta_t + E_{\alpha,\beta}|$, the thermally excited states are found at $eV_{\pm\alpha^*,\pm\beta^*} = \mp|\Delta_t - E_{\alpha,\beta}|$ [16]. The thermally excited YSR states are of much less intensity and, therefore, exhibit a small or negligible region of NDC. Figure S14 shows the dI/dV maps recorded at the corresponding voltages of the thermally excited YSR states for atoms I-VI. In these maps the similarity of the $\pm\beta^*$ states of atoms I, II and IV is more striking than in the original maps of $\pm\beta$. To illustrate the impact of the NDC from the $\pm\alpha$ -YSR resonances on the $\pm\beta$ state, we simulate the map of $\pm\beta$ by subtracting a fraction of the $\pm\alpha$ maps (mimicking the NDC) from the $\pm\beta^*$ maps. The result is compared to the maps at the energies corresponding to $\pm\beta$ (Fig. S15) and shows remarkable similarity, illustrating the impact of NDC.

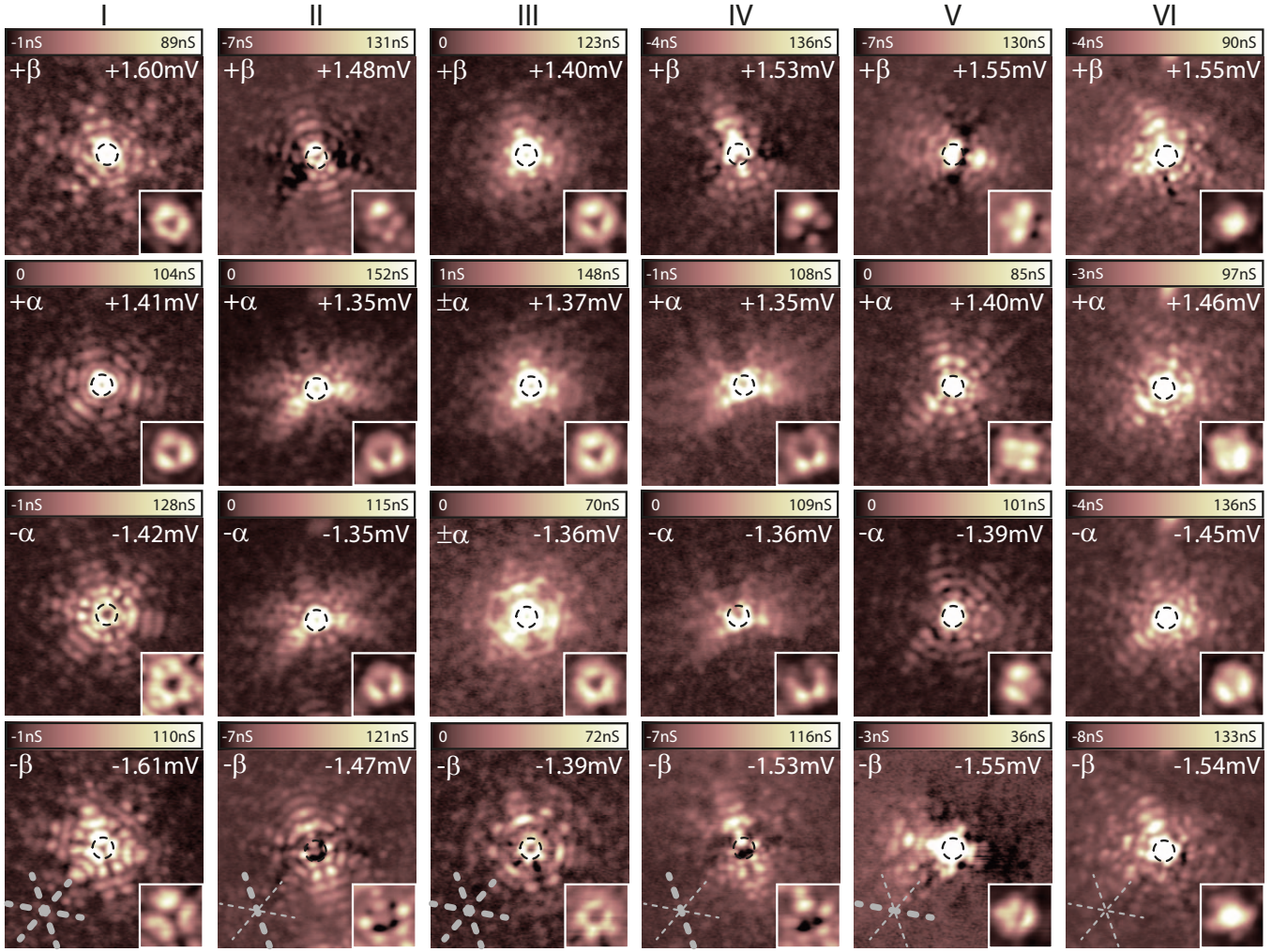


Figure S13. Constant-current dI/dV maps ($9.5 \times 9.5 \text{ nm}^2$) of the YSR ($\pm\alpha, \pm\beta$) states of HC atoms I-VI (set point: 4 mV, 200 pA; $V_{\text{rms}} = 15\text{-}25 \text{ } \mu\text{eV}$; V_{bias} as indicated in the images). The insets show a $2 \times 2 \text{ nm}^2$ close-up view around the center of the atoms. Black dashed circles (diameter 1 nm) outline the atoms' position. The grey dashed lines in the bottom map of each atom indicate the crystal's symmetry axes. Thick lines indicate mirror axes present in the dI/dV map.

Determination of YSR energies

To determine the YSR energies, we fit the deconvolved spectra [*cf.* Eqs. (S21) and (S22)] in the low-energy region with a set of 4 Gaussians (2 pairs of peaks):

$$\text{LDOS}(E) = D_0 + A_1 e^{-(E-E_\alpha)^2/(2\sigma^2)} + A_2 e^{-(E+E_\alpha)^2/(2\sigma^2)} + B_1 e^{-(E-E_\beta)^2/(2\sigma^2)} + B_2 e^{-(E+E_\beta)^2/(2\sigma^2)}. \quad (\text{S23})$$

Here, D_0 is an offset, E_α and E_β are the YSR energies, $A_{1,2}$ and $B_{1,2}$ are four amplitudes and σ is the width of the Gaussian peaks.

The top panel of Fig. S16c shows the extracted energies of the YSR states of approximately 90 atoms with respect to their location relative to the CDW. The error bar in x-direction results from the inaccuracy in finding the exact position relative to the CDW as discussed along with Fig. S10. The error margins of the YSR energy include the uncertainty in the exact value of the tip's energy gap Δ_t , the lock-in modulation of the bias voltage and the standard deviation of the fit routine. Additionally, an error of $\pm\sigma/2$ was added to the energy uncertainty if the peaks are not well separated (*i.e.* $E_\alpha - E_\beta \leq 2\sigma$). This is mainly the case for atoms close to the CDW minimum, where we cannot distinguish the α - and β -resonances as they are both very close to zero energy (*e.g.* atom III in the main text). Some of these atoms can be fitted with only one pair of Gauss peaks as the YSR states overlap. In this case both energies have the same value ($E_\alpha = E_\beta$).

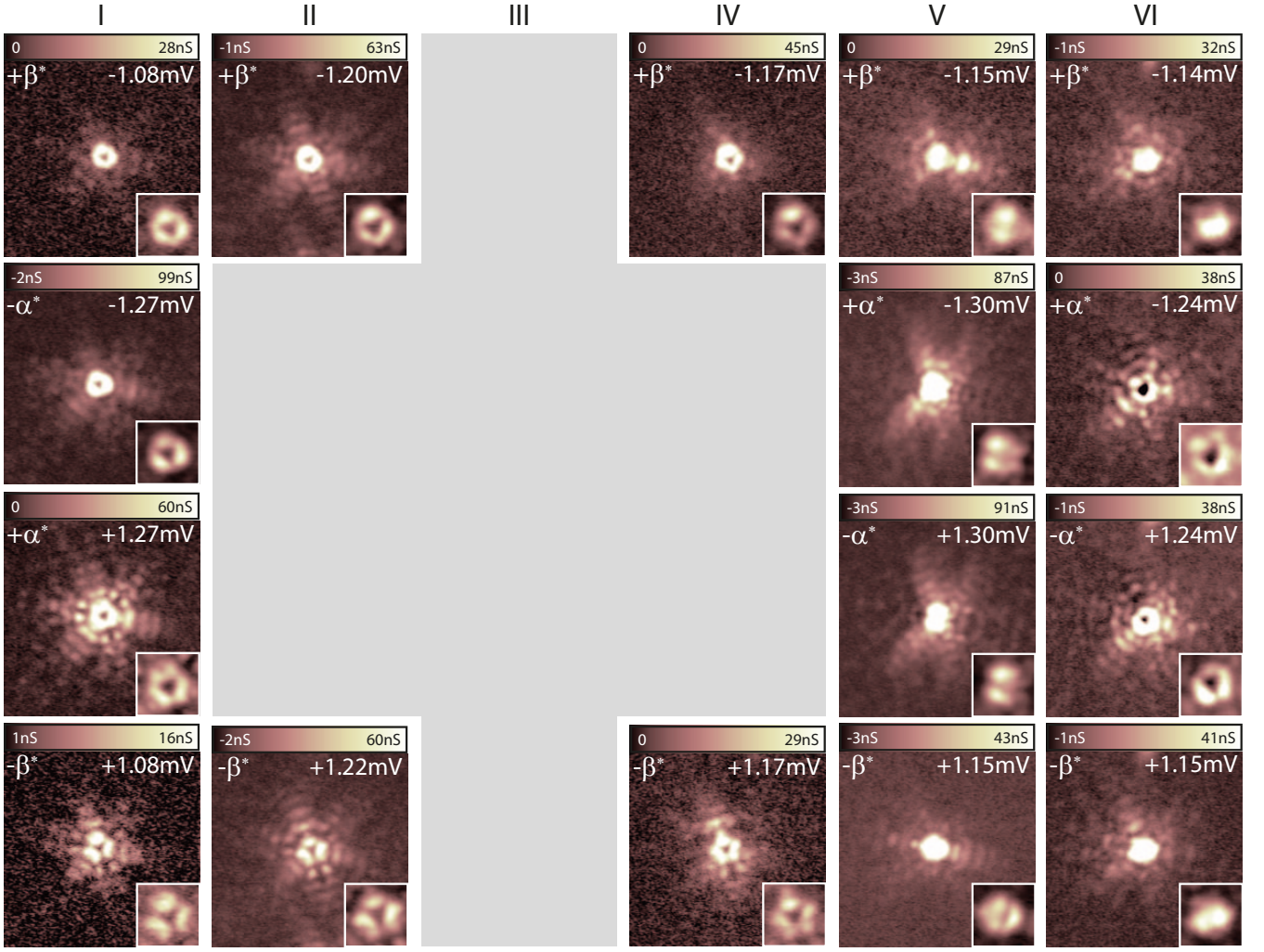


Figure S14. Constant-current dI/dV maps ($9.5 \times 9.5 \text{ nm}^2$) of the thermally excited YSR ($\pm\alpha, \pm\beta$) states (set point: 4 mV, 200 pA; $V_{\text{rms}} = 15\text{-}25 \mu\text{eV}$; V_{bias} as indicated in the images). The insets show a $2 \times 2 \text{ nm}^2$ close-up view around the center of the atoms. The images are arranged in the same way as in Fig. S13, *i.e.* the maps of the thermally excited YSR states can be found in the same position within the array as in Fig. S13. For YSR resonances at zero energy (*i.e.* $eV_{+\beta} = eV_{-\beta} = \Delta_t$) there are no maps of the corresponding thermal excitations (grey area).

As discussed in the main manuscript, we find a correlation of the YSR energy with position along the CDW symmetry axis. E_α and E_β are largest at the maximum of the CDW and decrease with distance from the maxima. By default, the fit outputs for E_α and E_β are positive. Assuming that E_α and E_β should follow a similar trend, we suggest that the α -resonance crosses zero energy, *i.e.* undergoes the quantum phase transition [26]. Therefore, $E_\alpha < 0$ was assumed for the atoms in close vicinity to the CDW minimum (*cf.* atom III, the set of atoms with $E_\alpha < 0$ is marked in orange and grey). Having passed the minimum (*cf.* atom IV) the α - and β -states can be separated and identified again in the dI/dV maps (see Fig. 3 in the main manuscript and Figs. S13, S14, S15), *i.e.* $E_\alpha > 0$.

The top panel of Fig. 4a in the main manuscript is obtained from the data in Fig. S16c by averaging over all atoms that are found within an interval of $\pm 0.05 a_{\text{cdw}}$. This corresponds to the uncertainty in the determination of the atoms' position with respect to the CDW (see above). The error margins in energy are the standard deviations of the averaging including the average of the errors shown in Fig. S16c.

-
- [1] G. Grüner, *Density waves in solids* (CRC Press, 1994).
 - [2] N. V. Smith, S. D. Kevan, and F. J. DiSalvo, *J. Phys. C: Solid State Phys.* **18**, 3175 (1985).

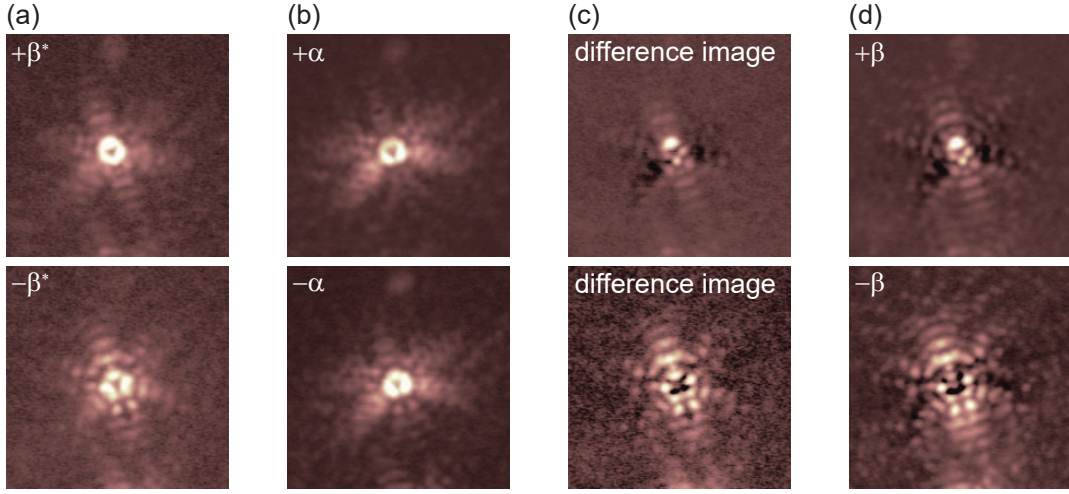


Figure S15. Constant-current dI/dV maps of (a) $+\beta^*$ (top) and $-\beta^*$ (bottom) of atom II (same data can be found in Fig. S14), and (b) $+\alpha$ (top) and $-\alpha$ (bottom) of atom II (same data can be found in Fig. S13). (c) Difference images: $+\alpha$ ($-\alpha$) map subtracted with a factor of 0.7 (1.0) from the map $+\beta^*$ ($-\beta^*$). (d) dI/dV map of the $+\beta$ (top) and $-\beta$ (bottom) resonance (same data can be found in Fig. S13). (c) and (d) are very similar.

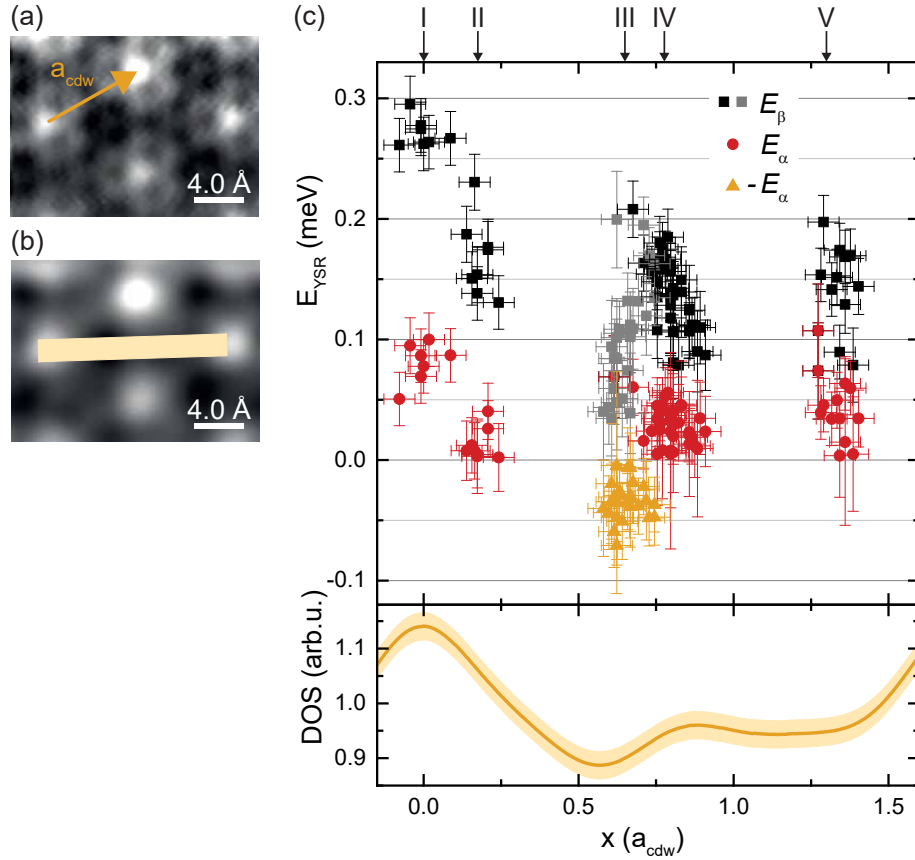


Figure S16. (a) Constant-height dI/dV map taken at $T = 8$ K and $V_{\text{bias}} = 0$ (set point 4 mV, 200 pA; $V_{\text{rms}} = 100$ μeV ; some z -drift is visible). (b) FFT-filtered data of (a). The signal averaged over the radius of influence of 125 pm, which is approx. the covalent radius of a Fe atom (yellow shaded area) is plotted in the bottom panel of (c) for one complete period of the CDW. (c) Evaluation of YSR energies E_α , E_β of approximately 90 atoms measured on several samples with several Pb tips by fitting the deconvolved spectra as described in the text. Error bars are also discussed in the text. Black and grey show the evolution of E_β . Red and orange data points correspond to E_α . For the orange data points a negative E_α was assumed.

- [3] K. Rossnagel, E. Rotenberg, H. Koh, N. V. Smith, and L. Kipp, [Phys. Rev. B **72**, 121103 \(2005\)](#).
- [4] D. S. Inosov, V. B. Zabolotnyy, D. V. Evtushinsky, A. A. Kordyuk, B. Büchner, R. Follath, H. Berger, and S. V. Borisenko, [New J. Phys. **10**, 125027 \(2008\)](#).
- [5] D. S. Inosov, D. V. Evtushinsky, V. B. Zabolotnyy, A. A. Kordyuk, B. Büchner, R. Follath, H. Berger, and S. V. Borisenko, [Phys. Rev. B **79**, 125112 \(2009\)](#).
- [6] D. J. Rahn, S. Hellmann, M. Kalläne, C. Sohrt, T. K. Kim, L. Kipp, and K. Rossnagel, [Phys. Rev. B **85**, 224532 \(2012\)](#).
- [7] G. C. Ménard, S. Guissart, C. Brun, S. Pons, V. S. Stolyarov, F. Debontridder, M. V. Leclerc, E. Janod, L. Cario, D. Roditchev, P. Simon, and T. Cren, [Nat. Phys. **11**, 1013 \(2015\)](#).
- [8] L. Bawden, S. P. Cooil, F. Mazzola, J. M. Riley, L. J. Collins-McIntyre, V. Sunko, K. W. B. Hunvik, M. Leandersson, C. M. Polley, T. Balasubramanian, T. K. Kim, M. Hoesch, J. W. Wells, G. Balakrishnan, M. S. Bahramy, and P. D. C. King, [Nature Comm. **7**, 11711 \(2016\)](#).
- [9] X. Xi, Z. Wang, W. Zhao, J.-H. Park, K. T. Law, H. Berger, L. Forró, J. Shan, and K. F. Mak, [Nat. Phys. **12**, 139 \(2016\)](#).
- [10] C. P. Moca, E. Demler, B. Jankó, and G. Zaránd, [Phys. Rev. B **77**, 174516 \(2008\)](#).
- [11] G. Kiršanskas, M. Goldstein, K. Flensburg, L. I. Glazman, and J. Paaske, [Phys. Rev. B **92**, 235422 \(2015\)](#).
- [12] M. Ruby, Y. Peng, F. von Oppen, B. W. Heinrich, and K. J. Franke, [Phys. Rev. Lett. **117**, 186801 \(2016\)](#).
- [13] L. Yu, [Acta Phys. Sin. **21**, 75 \(1965\)](#).
- [14] H. Shiba, [Prog. Theor. Phys. **40**, 435 \(1968\)](#).
- [15] A. I. Rusinov, [JETP Lett. **9**, 85 \(1969\)](#).
- [16] M. Ruby, F. Pientka, Y. Peng, F. von Oppen, B. W. Heinrich, and K. J. Franke, [Phys. Rev. Lett. **115**, 087001 \(2015\)](#).
- [17] J. Tersoff and D. R. Hamann, [Phys. Rev. B **31**, 805 \(1985\)](#).
- [18] M. Ruby, B. W. Heinrich, J. I. Pascual, and K. J. Franke, [Phys. Rev. Lett. **114**, 157001 \(2015\)](#).
- [19] D.-J. Choi, C. Rubio-Verdú, J. De Bruijckere, M. M. Ugeda, N. Lorente, and J. I. Pascual, [Nat. Commun. **8**, 15175 \(2017\)](#).
- [20] G. Gye, E. Oh, and H. W. Yeom, [Phys. Rev. Lett. **122**, 016403 \(2019\)](#).
- [21] F. Cossu, A. G. Moghaddam, K. Kim, H. A. Tahini, I. Di Marco, H.-W. Yeom, and A. Akbari, [Phys. Rev. B **98**, 195419 \(2018\)](#).
- [22] M. Langer, M. Kisiel, R. Pawlak, F. Pellegrini, G. E. Santoro, R. Buzio, A. Gerbi, G. Balakrishnan, A. Baratoff, E. Tosatti, and E. Meyer, [Nat. Mater. **13**, 173 \(2014\)](#).
- [23] F. Flicker and J. van Wezel, [Nat. Commun. **6**, 7034 \(2015\)](#).
- [24] U. Chatterjee, J. Zhao, M. Iavarone, R. Di Capua, J. P. Castellan, G. Karapetrov, C. D. Malliakas, M. G. Kanatzidis, H. Claus, J. P. C. Ruff, F. Weber, J. Van Wezel, J. C. Campuzano, R. Osborn, M. Randeria, N. Trivedi, M. R. Norman, and S. Rosenkranz, [Nat. Commun. **6**, 6313 \(2015\)](#).
- [25] C. J. Arguello, S. P. Chockalingam, E. P. Rosenthal, L. Zhao, C. Gutiérrez, J. H. Kang, W. C. Chung, R. M. Fernandes, S. Jia, A. J. Millis, R. J. Cava, and A. N. Pasupathy, [Phys. Rev. B **89**, 235115 \(2014\)](#).
- [26] K. J. Franke, G. Schulze, and J. I. Pascual, [Science **332**, 940 \(2011\)](#).